MTSS1 Regulation of Actin-Nucleating Formin DAAM1 in Dendritic Filopodia Determines Final Dendritic Configuration of Purkinje Cells

AUTHOR(S):

Kawabata Galbraith, Kelly; Fujishima, Kazuto; Mizuno, Hiroaki; Lee, Sung-Jin; Uemura, Takeshi; Sakimura, Kenji; Mishina, Masayoshi; Watanabe, Naoki; Kengaku, Mineko

CITATION:

Kawabata Galbraith, Kelly ...[et al]. MTSS1 Regulation of Actin-Nucleating Formin DAAM1 in Dendritic Filopodia Determines Final Dendritic Configuration of Purkinje Cells. Cell Reports 2018, 24(1): 95-106.e9

ISSUE DATE:

2018-07-03

URL:

http://hdl.handle.net/2433/232641

Article

Cell Reports

MTSS1 Regulation of Actin-Nucleating Formin DAAM1 in Dendritic Filopodia Determines Final Dendritic Configuration of Purkinje Cells

Graphical Abstract

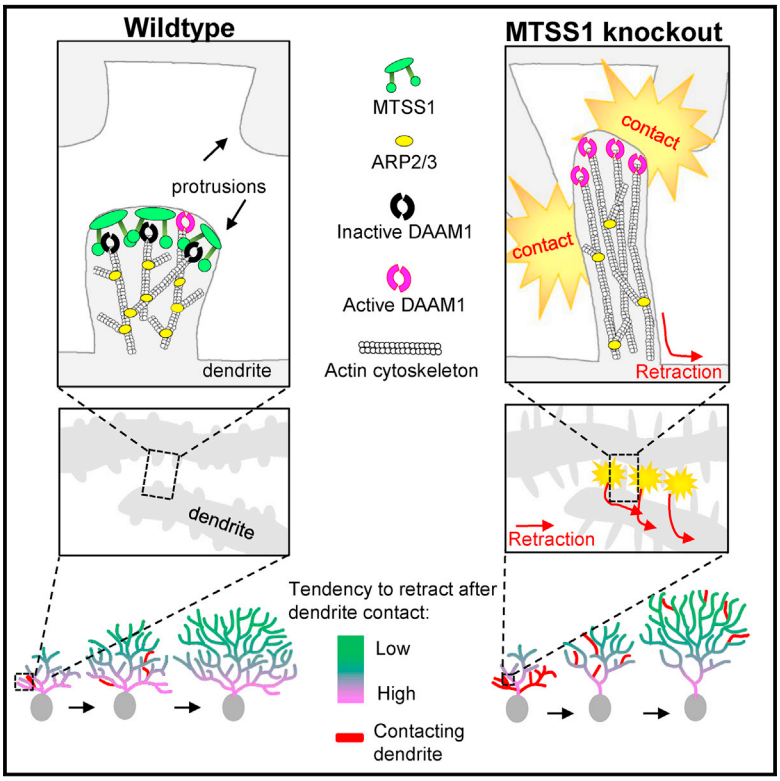

Authors

Kelly Kawabata Galbraith, Kazuto Fujishima, Hiroaki Mizuno, ..., Masayoshi Mishina, Naoki Watanabe, Mineko Kengaku

Correspondence

kengaku@icems.kyoto-u.ac.jp

In Brief

Kawabata Galbraith et al. demonstrate MTSS1's function at the intersection of two major actin-nucleating pathways, ARP2/3 and formins, in the dendritic protrusions of Purkinje cells. Loss of MTSS1 critically impacts actin-based microstructure morphology and ultimately the final structure of the dendritic arbor.

Highlights

- MTSS1 loss decreases dendritic arbor complexity in cerebellar Purkinje cells
- MTSS1 loss increases branch retraction by contact of longer dendritic protrusions
- Dendritic protrusion shape is governed by competition between ARP2/3 and formins
- MTSS1 directly inhibits actin nucleation by the formin DAAM1 in dendritic protrusions

Kawabata Galbraith et al., 2018, Cell Reports *24*, 95–106
July 3, 2018
https://doi.org/10.1016/j.celrep.2018.06.013

CellPress

Cell Reports
Article

MTSS1 Regulation of Actin-Nucleating Formin DAAM1 in Dendritic Filopodia Determines Final Dendritic Configuration of Purkinje Cells

Kelly Kawabata Galbraith,[1,2] Kazuto Fujishima,[1] Hiroaki Mizuno,[2] Sung-Jin Lee,[4] Takeshi Uemura,[4] Kenji Sakimura,[5] Masayoshi Mishina,[4,6] Naoki Watanabe,[2,3] and Mineko Kengaku[1,2,7,*]
[1]Institute for Integrated Cell-Material Sciences (WPI-iCeMS), Kyoto 606-8501, Japan
[2]Graduate School of Biostudies, Kyoto University, Kyoto 606-8501, Japan
[3]Graduate School of Medicine, Kyoto University, Kyoto 606-8501, Japan
[4]Department of Molecular Neurobiology and Pharmacology, Graduate School of Medicine, University of Tokyo, Tokyo 113-0033, Japan
[5]Department of Cellular Neurobiology, Brain Research Institute, Niigata University, Niigata 951-8585, Japan
[6]Brain Science Laboratory, The Research Organization of Science and Technology, Ritsumeikan University, Shiga 525-8577, Japan
[7]Lead Contact
*Correspondence: kengaku@icems.kyoto-u.ac.jp
https://doi.org/10.1016/j.celrep.2018.06.013

SUMMARY

Dendritic filopodia of developing neurons function as environmental sensors, regulating the spatial organization of dendrites and proper targeting to presynaptic partners. Dendritic filopodia morphology is determined by the balance of F-actin assembled via two major nucleating pathways, the ARP2/3 complex and formins. The inverse-BAR protein MTSS1 is highly expressed in Purkinje cells (PCs) and has been shown to upregulate ARP2/3 activity. PCs in MTSS1 conditional knockout mice showed dendrite hypoplasia due to excessive contact-induced retraction during development. This phenotype was concomitant with elongated dendritic filopodia and was phenocopied by overactivation of the actin nucleator formin DAAM1 localized in the tips of PC dendritic protrusions. Cell biology assays including single-molecule speckle microscopy demonstrated that MTSS1's C terminus binds to DAAM1 and paused DAAM1-mediated F-actin polymerization. Thus, MTSS1 plays a dual role as a formin inhibitor and ARP2/3 activator in dendritic filopodia, determining final neuronal morphology.

INTRODUCTION

Dendritic arbor size, shape, and location critically affect synaptic integration and neuronal circuit organization. Dendrites of space-filling arbors allow for maximum coverage of a field while minimizing inefficient redundancies (Parrish et al., 2007; Snider et al., 2010). Recent studies have shown contact-dependent stalling and/or retraction of growing branches as one mechanism to achieve such morphology (Han et al., 2012; Smith et al., 2012). The cell-surface molecules involved in dendritic self-avoidance of space-filling neurons have only recently been identified in the mammalian nervous system, including DSCAM (Fuerst et al., 2009), Semaphorin 6A (Sun et al., 2013), γ-protocadherins (Lefebvre et al., 2012), and Robo2/Slit2 (Gibson et al., 2014). However, it remains unclear how the signaling threshold for retraction and inter-dendrite spacing is established.

We have previously shown that dendritic protrusions, which encompass filopodia and immature spines, mediate contact-dependent stalling and retraction of Purkinje cell (PC) dendrites to achieve its large space-filling configuration (Fujishima et al., 2012). Dendritic protrusions vary considerably in shape, dynamics, and internal organization by changes in the underlying actin cytoskeleton, depending on developmental stage, activity, and disease state (Hotulainen and Hoogenraad, 2010; Yuste and Bonhoeffer, 2004), and have been shown to contain unbundled, bidirectional arrangements of F-actin (Hotulainen et al., 2009; Korobova and Svitkina, 2010). The rate-limiting step of F-actin assembly is mediated by two major classes of actin nucleators: the ARP2/3 complex forms a branched F-actin network, whereas formins such as mDia1 (Campellone and Welch, 2010) and DAAM1 (Jaiswal et al., 2013) can form linear, unbranched F-actin and mediate polymerization by remaining associated with the growing barbed end. In contrast to canonical filopodia consisting of formin-dependent unbranched F-actin, dendritic protrusions contain both actin nucleators (Korobova and Svitkina, 2010). Thus, with their small volumes and dynamic morphology, dendritic protrusions require tight control of actin nucleators to achieve correct morphological structure (Miermans et al., 2017; Hotulainen et al., 2009; Spence et al., 2016); yet, how these pathways are temporally and locally balanced in dendritic protrusions is not well understood.

Metastasis suppressor-1 (MTSS1, also known as MIM) is a member of the inverse-Bin/Amphiphysin/Rvs domain (I-BAR) superfamily highly expressed in the developing central nervous system (Mattila et al., 2003). The N-terminal membrane-binding I-BAR domain self-associates to form a homodimer and induces protrusion of the plasma membrane (Suetsugu et al., 2006). MTSS1 is known to directly bind to G-actin with high affinity via its C-terminal Wiskott-Aldrich syndrome protein (WASP) homology 2 (WH2) domain (Mattila et al., 2003; Woodings et al.,

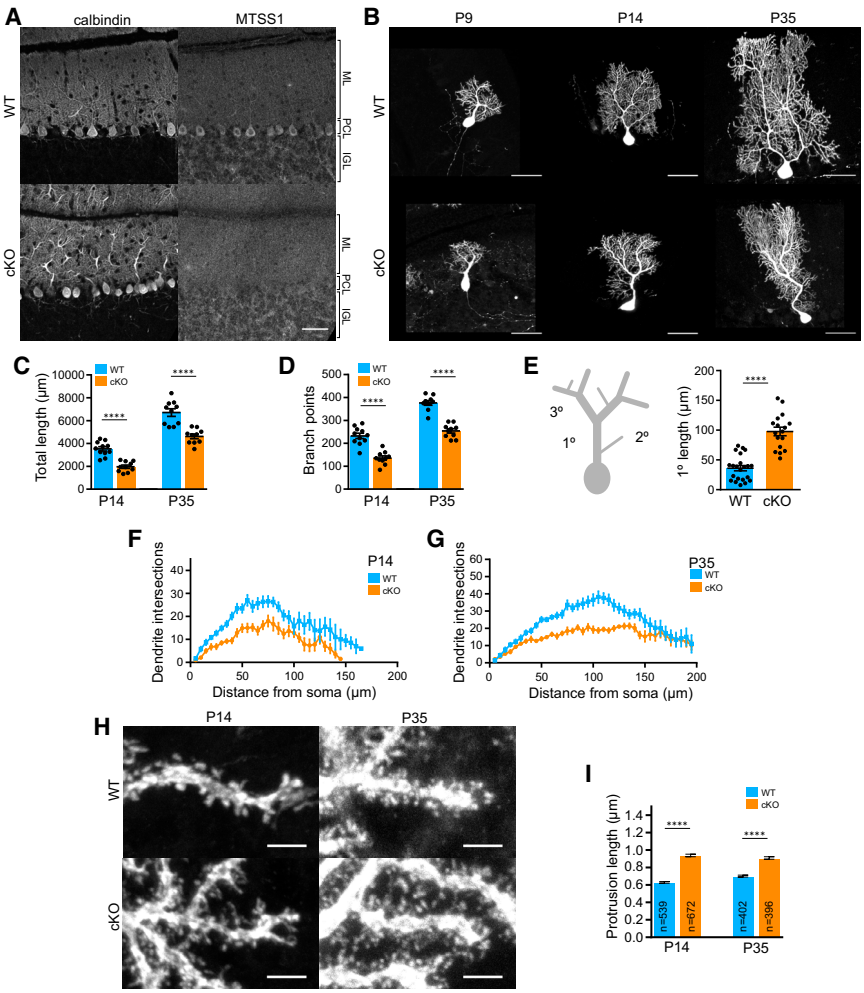

Figure 1. Purkinje-Specific Loss of MTSS1 Results in Decreased Dendritic Complexity and Increased Dendritic Protrusion Length *In Vivo*

(A) Endogenous staining of PC marker calbindin and MTSS1 in sagittal cerebellar sections from WT (top) and cKO (bottom) mice at P7. IGL, internal granule layer; ML, molecular layer; PCL, Purkinje cell layer.

(B) Representative images of PCs labeled with AAV-GFP in sagittal cerebellar sections from WT (top) and cKO (bottom) mice at indicated ages.

(C and D) Quantification of total dendritic length (C) and total number of branch points (D) from AAV-GFP-labeled PCs at indicated ages reconstructed and traced using Imaris software. n = 10–11 neurons per condition.

(E) Diagram illustrating PC dendrite classification and quantification of primary dendrite length in mature PCs (P35). N ≥ 17 neurons per condition.

(F and G) Sholl analyses of AAV-GFP-labeled PCs reconstructed in Imaris software at ages P14 (F) and P35 (G). The number of dendrites intersecting concentric circles centered at the point of primary dendrite emanation from the soma with increasing radii was measured at an increment of 5 μm. n = 9–11 neurons per condition.

(H) Distal dendrites and their dendritic protrusions at indicated ages in WT and cKO PCs labeled with AAV-GFP.

(I) Quantification of distal dendritic protrusion length in WT and cKO PCs.

All data show mean ± SEM. Scale bars, 50 μm (A, B); 3 μm (H). ****p < 0.0001. See also Figure S1.

2003), as well as upregulate the activity of ARP2/3 via multiple mechanisms (Lin et al., 2005; Saarikangas et al., 2015). It has also been demonstrated that MTSS1 interacts with a formin DAAM1 and regulates neural tube closure in *Xenopus* (Liu et al., 2011). DAAM1 has been shown to regulate filopodia formation via its processive actin polymerization activities (Jaiswal et al., 2013). A more recent study using MTSS1 null mice has demonstrated for the first time that MTSS1 regulates dendritic protrusion initiation in neurons by coupling I-BAR-dependent plasma membrane bending and ARP2/3-mediated actin polymerization (Saarikangas et al., 2015). Furthermore, MTSS1 null mice have altered synaptic transmission at PC spines and progressive neurological and behavioral deficits that are associated with the cerebellum and other brain regions expressing MTSS1 (Saarikangas et al., 2015; Sistig et al., 2017). However, the causal link between the molecular function and loss-of-function cellular phenotypes remains ambiguous.

Using conditional knockout (cKO) mice lacking MTSS1 in PCs, we demonstrate that MTSS1 loss results in dendritic hypoplasia and show that MTSS1 determines dendritic protrusion length and the threshold for branch retraction, thereby influencing the complexity of the space-filling dendrites. We provide evidence that the C terminus of MTSS1 binds to and inhibits actin assembly by DAAM1 in dendritic protrusions in neurons. Thus, we identify MTSS1's dual role in regulating a formin as well as ARP2/3, pointing to the importance of coordinating the precise balance of diverse actin assembly strategies during neuronal morphogenesis.

RESULTS

PC-Specific MTSS1 Knockout Results in Loss of Dendritic Arbor Complexity

We sought to clarify the cell-autonomous function of MTSS1 in PC morphogenesis using a PC-specific MTSS1 knockout mouse (cKO, *GluRδ2-Cre; Mtss1$^{flox/flox}$*) (Figures S1A–S1D). We generated an *Mtss1$^{flox/flox}$* mouse, which was then crossed with a Cre line under the control of the GluRδ2 promoter (*GluRδ2-Cre*); this promoter is restricted to PCs and starts expression at embryonic day 15 (Takayama et al., 1996). Clear abolishment of MTSS1 signal in PCs was confirmed by post-natal day (P) 7 (Figure 1A) and in adults (Figure S1E). Loss of MTSS1 did not disrupt the cerebellar cortical layer organization or molecular layer height (Figures S1F and S1G).

To analyze the morphology of individual PCs, P1 pups underwent intracerebellar injection of adeno-associated virus (AAV)

carrying a GFP expression construct, and PCs were analyzed at the indicated ages. Compared with wild-type (WT, *Mtss1*$^{flox/flox}$) PCs, loss of MTSS1 in cKO PCs reduced complexity in dendritic branching as early as P9 (Figure 1B). By P14, in which PCs are actively forming new dendrites (Kaneko et al., 2011), cKO PCs showed an ~40% decrease in both total dendritic length (WT, 3,530 ± 189 μm; cKO, 1,970 ± 142 μm; mean ± SEM) and branch points (WT, 233 ± 11; cKO, 136 ± 9) (Figures 1C and 1D). By P35, at which stage PCs are finished growing, cKO PCs showed a still significant ~30% reduction in dendritic complexity (total dendritic length: WT, 6,710 ± 330 μm; cKO, 4,620 ± 203 μm; branch points: WT, 377 ± 10; cKO, 254 ± 10). By maturation at P35, cKO PCs had many smaller, thinner dendrites emanating from a longer, thick primary dendrite that bifurcated far from the soma (WT, 36 ± 4 μm; cKO, 98 ± 7 μm) (Figure 1E). Furthermore, Sholl analysis demonstrated that dendrite density was reduced proximal to the soma in cKO PCs, although density at distal regions approached WT levels by maturation (Figures 1F and 1G). Interestingly, we observed that the primary dendrites of cKO PCs were positioned within the molecular layer at non-uniform and bent angles, presumably to compensate for the loss of proximal dendrites (Figure S1G).

Close observation of subcellular structures revealed that dendritic protrusions in P14 cKO PCs looked thinner, as previously reported (Saarikangas et al., 2015). However, unlike previous observations, we detected no obvious change in protrusion density in cKO PCs, although precise quantification was technically challenging because of the high density of dendritic protrusions (Figures 1H and 1I). The dendritic protrusions were longer than those of WT PCs (WT, 0.63 ± 0.01 μm; cKO, 0.94 ± 0.01 μm), which could be observed until P35 (WT, 0.70 ± 0.01 μm; cKO, 0.91 ± 0.01 μm).

MTSS1 Knockout PCs Show Increased Early-Stage Contact-Dependent Dendritic Retraction *In Vitro*

To better observe the developmental characteristics of cKO PCs, we performed *in vitro* cultures of dissociated cerebellar cells from P0.5 pups. Like *in vivo* PCs, cKO PCs *in vitro* showed a similar loss of dendritic complexity (Figure 2A). At 12 days *in vitro* (DIV) (12DIV), cKO PCs showed an ~60% decrease in total dendritic length and ~55% decrease in branch points (Figures 2B and 2C). Furthermore, cKO PCs showed a 46% decrease in the number of primary dendrites. To address whether the loss of dendrite complexity in MTSS1-deficient PCs was due to decreased dendrite formation or increased retraction frequency, we performed time-lapse imaging of PCs during their period of dendritic arborization. Like WT neurons, cKO PCs started growth with multiple primary dendrites with frequent extension of dendrites; however, these dendrites were often retracted within 24 hr (Figures 2E and 2F; Video S1). Throughout development, cKO PCs showed more retractions than WT PCs, particularly in the beginning stages of dendritic arborization (Figure 2G). Time-dependent Sholl analyses showed the progressive loss of proximal dendrites in cKO PCs, which are established first during development (Figures 2H and 2I). We confirmed that dendritic growth speed was not decreased but rather increased in cKO PCs (Figure S2A). Branching probability remained unchanged until 10DIV, yet decayed at 11DIV in WT cells and remained high in cKO (Figure S2B). It is thus unlikely that the dendritic hypoplasia is due to decreased dendrite formation. This phenotype is similar to that observed *in vivo*, suggesting that the resulting morphology is established by increased proximal dendrite retraction during the early stages of dendritic arborization.

Length of Dendritic Protrusions Regulates Final PC Dendritic Morphology

The growing dendrites of cultured PCs at 12DIV are stubbed with dendritic protrusions that include both filopodia and thin, headed spines (Lee et al., 2004; Shimada et al., 1998). Consistent with *in vivo* observations, the average length of dendritic protrusions in cKO PCs was significantly increased (WT, 0.98 ± 0.02 μm; cKO, 1.60 ± 0.03 μm), as was the distribution of lengths (Figures 2J and 2K). Time-lapse imaging showed dynamic extension and retraction of dendritic protrusions in cKO PCs, with some filopodia-like protrusions reaching up to 4 μm and retracting again (Video S2). These results suggested a mechanism in which the length of dendritic protrusions, which are the first point of contact with surrounding growing dendrites, may increase the frequency of encountering a retraction stimulus and may underlie the dendritic morphology observed in cKO PCs. To test this hypothesis, we used a previously established computer model of PC dendritic arbor growth based on morphological parameters, dendritic growth speed, and branching and retraction probabilities (Fujishima et al., 2012). Setting the parameters as previously reported, the distribution of the simulated growing dendrites reflected that of PCs grown *in vitro* (Figure 2L). When the average length of dendritic protrusions was increased by 0.6 μm, reflecting the average length increase observed in culture, and all other parameters kept constant, simulated neurons showed reduced dendritic branching (Figures 2M and 2N) and a 32% decrease in primary dendrite count (Figure 2O). The average morphology of neurons simulated with longer filopodia showed similar loss of branches in proximal regions consistent with experimental observations. These results suggest that regulation of length of dendritic protrusions is important for space-filling neurons to achieve their final morphology.

The C Terminus of MTSS1 Regulates the Length of Dendritic Protrusions and Proper Dendritic Arborization in PCs

The I-BAR domain of MTSS1 has been well studied for its membrane-bending activity, accumulation of PIP_2, and regulation of the GTPase Rac1, and it has been shown to have distinct functions in initiating canonical filopodia and spine precursors (Bompard et al., 2005; Mattila et al., 2007; Saarikangas et al., 2015). On the other hand, the C terminus of MTSS1 includes the WH2 domain, which has been shown to bind G-actin (Mattila et al., 2003; Woodings et al., 2003), and serine-rich (SRD) and proline-rich domains (PRD), which regulate other actin-binding proteins (Lin et al., 2005; Liu et al., 2011; Quinones et al., 2010). To understand the mechanistic function of MTSS1 in the regulation of PC dendritic arbor and protrusion morphology, several GFP-tagged MTSS1 truncate proteins (Figures 3A and S3A) were generated and transfected into cerebellar cultures at 0DIV.

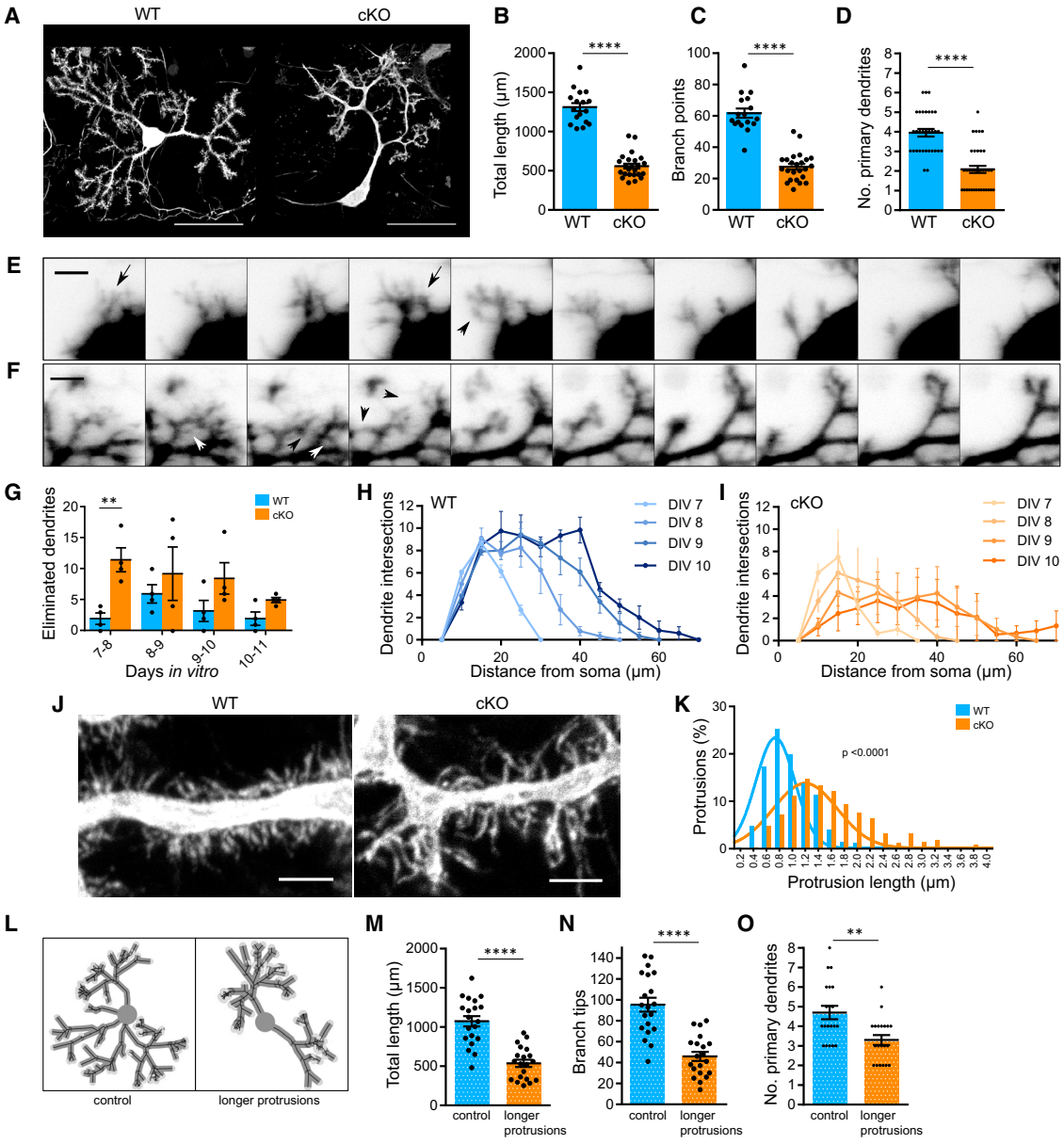

Figure 2. MTSS1 Knockout PCs Show Increased Early-Stage Contact-Dependent Dendritic Retraction *In Vitro* Caused by Increased Dendritic Protrusion Length

(A) Representative images of PCs transfected with GFP in dissociated cerebellar cultures of WT (left) and cKO (right) mice at 12DIV.

(B–D) Quantification of total dendritic length (B), number of branch points (C), and primary dendrites (D). n = 17–24 neurons per condition.

(E and F) Montages of time-lapse imaging started at 7DIV of developing dendrites from one cKO PC (E) and another example (F) labeled with AAV-GFP in dissociated cerebellar culture. Figures show progression every 6 hr. Arrows indicate apparent collisions of dendritic branches.

(G) Quantification of eliminated dendrite events observed during time-lapse imaging of PCs. One event was counted on the last frame of retraction. n = 4 neurons per condition.

(H and I) Time-dependent Sholl analyses of developing PCs in WT (H) and cKO (I) cultures observed during time-lapse imaging. n = 4 per condition.

(J) Representative images of dendritic segments from PCs transfected with GFP in dissociated WT (left) and cKO (right) cerebellar cultures at 12DIV.

(K) Distribution of WT (n = 540) and cKO (n = 572) dendritic protrusion lengths in 12DIV PCs.

(L) Representative image of computer-simulated PCs using WT (left) and increased dendritic protrusion length (right) parameters.

(M–O) Quantification of total dendritic length (M), number of branch points (N), and primary dendrites (O) of computer-simulated neurons at 72 hr. n = 20 neurons precondition.

All data show mean ± SEM. Scale bars, 50 μm (A); 10 μm (E and F); 3 μm (J). **p < 0.01; ***p < 0.001; ****p < 0.0001. See also Figure S2 and Videos S1 and S2.

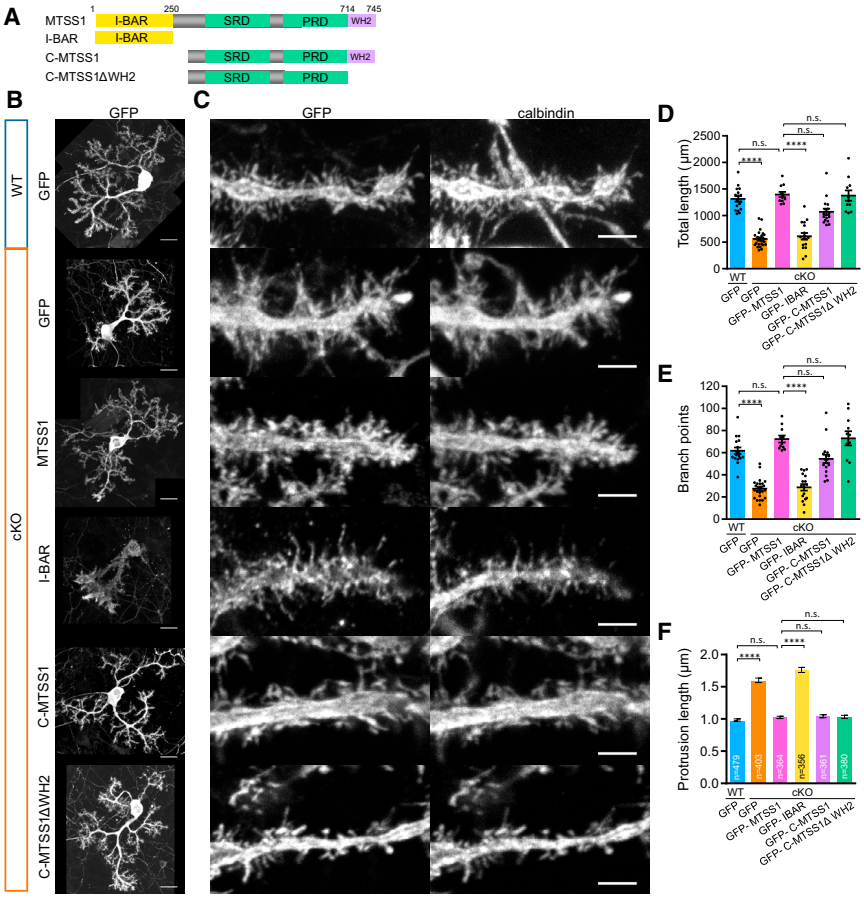

Figure 3. The C Terminus of MTSS1 Regulates the Length of Dendritic Protrusions and Proper Dendritic Arborization in Purkinje Cells

(A) Schematic of MTSS1 domains and constructs.

(B) Representative images showing GFP signal of 12DIV WT and cKO PCs in dissociated cerebellar cultures, transfected at 0DIV with GFP or GFP-MTSS1 constructs.

(C) Representative GFP and calbindin images of dendritic segments from PCs described in (B).

(D and E) Quantification of total dendritic length (D) and total number of branch points (E). n = 11–24 neurons per condition.

(F) Quantification of dendritic protrusion lengths. All data show mean ± SEM. Scale bars, 20 μM (B); 3 μM (C). ****p < 0.0001. See also Figure S3.

Analysis at 12DIV showed that overexpression of full-length MTSS1 completely rescued cKO dendritic arbor complexity, with comparable morphology to WT cells. Unexpectedly, expression of the I-BAR domain, which was localized strongly at the plasma membrane at more distal regions of the arbor, could not rescue dendritic growth (Figures 3B, 3D, and 3E). On the other hand, a similar expression level of C-MTSS1 (Figures S3A and S3B) was sufficient in rescuing PC dendritic arborization. Furthermore, complete rescue of dendritic arbor shape with C-MTSS1ΔWH2 demonstrated that this was independent of the strong G-actin binding activity of the WH2 domain.

At higher magnification, full-length GFP-MTSS1 was localized throughout the dendritic arbor and showed accumulation in dendritic protrusions (Figure 3C). cKO PCs expressing GFP-MTSS1 showed complete rescue in dendritic protrusion length (WT, 0.98 ± 0.02 μm; cKO+MTSS1, 1.02 ± 0.02) (Figure 3F). Dendritic protrusions in cKO PCs showed strong accumulation of GFP-I-BAR with long, very thin morphology and no rescue of protrusion length (1.76 ± 0.04 μm). Both GFP-C-MTSS1 and GFP-C-MTSS1ΔWH2 showed diffuse localization throughout the dendritic shaft and protrusions, and consistent with their rescue of the dendritic arbor, resulted in a rescue of dendritic protrusion length (C-MTSS1, 1.04 ± 0.02 μm; C-MTSS1ΔWH2, 1.03 ± 0.02 μm), indicating that the C-terminal SRD and PRD are critical for MTSS1 regulation of dendritic protrusion and arbor morphology.

MTSS1 Modulates Actin Nucleator Activity in PCs

Dendritic filopodia of developing neurons have been shown to contain branched and linear F-actin structures (Korobova and Svitkina, 2010), which are nucleated by the ARP2/3 complex and formin family, respectively. Using PCs, we first wanted to confirm previous reports that MTSS1 upregulated ARP2/3 activity in dendritic protrusions. We transfected dissociated WT cerebellar cultures with GFP-MTSS1 at 0DIV and observed at 12DIV numerous round, bulbous-shaped protrusions with slightly shorter length (WT, 1.02 ± 0.02 μm; WT+MTSS1, 0.89 ± 0.02 μm) (Figure 4A). Treatment with ARP2/3 inhibitor CK-666 (20 μM) led to a reduction in this morphology (Figure 4B), confirming that MTSS1 also positively regulates the ARP2/3 pathway in PCs. Of note, we observed that CK-666 treatment of control PCs resulted in a 57% increase in length of dendritic protrusions (WT+CK-666, 1.61 ± 0.03 μm), consistent with previous studies using RNAi to inhibit the activity of the ARP2/3 complex (Hotulainen et al., 2009; Kim et al., 2013; Spence et al., 2016). It is possible that this increase in length may be due to a shift to formin-dependent actin nucleation, because recent studies have shown that ARP2/3 and formin-mediated pathways of actin nucleation can compete for G-actin within cells (Rotty et al., 2015; Suarez et al., 2015). However, ARP2/3 inhibition of PCs overexpressing MTSS1 did not show the same magnitude of dendritic protrusion lengthening (WT + MTSS1 + CK-666, 1.13 ± 0.03 μm). This led us to wonder whether MTSS1 was negatively regulating formin activity.

To test this, we acutely treated 12DIV WT and cKO PC cultures with the pan-formin inhibitor SMI-FH2 (10 μM). Time-lapse imaging both before and after drug addition showed minor retraction of dendritic protrusions in WT cultures, but much more obvious retraction of the longer cKO dendritic protrusions (Figure 4C;

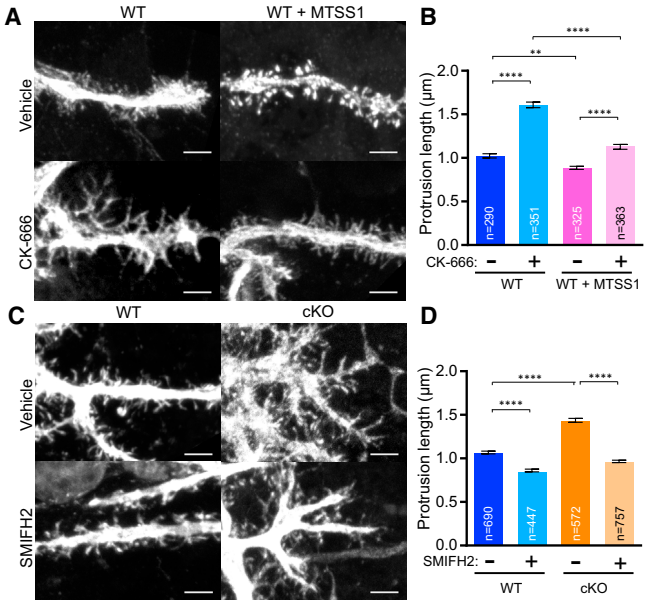

Figure 4. MTSS1 Modulates Actin Nucleator Activity in Purkinje Cells

(A) Representative images of 12DIV WT PCs transfected at 0DIV with either GFP (left) or GFP-MTSS1 (right) and treated with either vehicle (top) or 20 μm of the ARP2/3 inhibitor CK-666 for 24 hr prior to fixation.

(B) Quantification of dendritic protrusion lengths in PCs described in (A).

(C) Representative images of 12DIV WT (left) and cKO (right) PCs transfected at 0DIV with GFP and treated with either vehicle (top) or 10 μm of the formin inhibitor SMI-FH2 for 10 min prior to fixation.

(D) Quantification of dendritic protrusion lengths in PCs described in (C).

All data show mean ± SEM. Scale bars, 3 μm. $^{**}p < 0.01$; $^{****}p < 0.0001$. See also Video S3.

Video S3). Quantification of cultures fixed 10 min after drug application showed cKO dendritic protrusions decreased 33% in length, whereas WT protrusions showed a 19% decrease (Figure 4D). This rescue of cKO dendritic protrusion length suggested that loss of MTSS1 had resulted in the upregulation of formin activity. We were unable to observe whether pan-inhibition of formins by SMI-FH2 induces compensatory ARP2/3-dependent change in protrusion morphology because of the short treatment time required to avoid dendritic retraction.

DAAM1 Interacts with MTSS1 in Dendritic Protrusions and Regulates Protrusion Length

Because loss of MTSS1 led to an upregulation of formin activity in PC dendritic protrusions, we next aimed to identify which formin may be regulated by MTSS1 in PCs. In a previous report, the C-terminal SRD and PRD of MTSS1 were identified to bind to the catalytic domain of *Xenopus* DAAM1 (Liu et al., 2011). DAAM1 has been shown to be involved in many actin-dependent morphogenic developmental processes (Gombos et al., 2015; Matusek et al., 2008), as well as regulating filopodia formation (Hoffmann et al., 2014; Jaiswal et al., 2013). However, there have been no reports of DAAM1 involvement in neuronal dendritic protrusion formation. We first confirmed the presence of DAAM1 in developing mouse cerebellum (Figure 5A). Immunofluorescence of cultured WT PCs at 12DIV showed punctate somatodendritic localization of MTSS1 and strong DAAM1 localization in dendritic protrusions (Figures 5B and 5C). At higher magnified views, MTSS1 appeared to be at the tips of most protrusions (Figures 5D and 5E). DAAM1, on the other hand, showed variable distribution throughout the protrusion, with some long protrusions showing strong localization of DAAM1 at the tip. MTSS1 and DAAM1 colocalized or were closely apposed in most dendritic protrusions.

The actin nucleation and polymerization activities of DAAM1 have been shown to be mediated by its highly conserved catalytic domains (FH1 and FH2 domains) in the C terminus (Figure S4A). After confirming endogenous interaction of MTSS1 and DAAM1 in cerebellar lysates of developing mice at P8 (Figure 5F), we also sought for the domains of mammalian MTSS1-DAAM1 interaction by pull-down with purified GST-tagged MTSS1 truncates (Figures S4D–S4G). While the I-BAR domain of MTSS1 was unable to pull down GFP-C-DAAM1, both the C terminus of MTSS1 and C-MTSS1ΔWH2, which were shown to be entirely sufficient in rescuing the MTSS1 cKO morphological phenotype, showed interaction with C-DAAM1 (Figure S4E). We confirmed that MTSS1 did not bind to an analogous truncate of the well-characterized diaphanous-related formin mDia1, consistent with previous studies that showed specific interaction of MTSS1 with DAAM1, but not with an mDia1 isoform mDia2 in *Xenopus* (Liu et al., 2011) (Figure S4F).

We next examined whether MTSS1 regulates formin activity of DAAM1 in living cells. We confirmed that constitutively active C-DAAM1 increased F-actin content in NIH 3T3 cells, consistent with previous reports (Habas et al., 2001; Liu et al., 2008) (Figures 6A and 6B). In contrast, coexpression of MTSS1 significantly reduced C-DAAM1-induced actin assembly. These results suggest that MTSS1 negatively regulates DAAM1's actin-polymerizing activity.

We further explored whether the increased length of dendritic protrusions in MTSS1-deficient PCs is mediated by upregulation of DAAM1 activity. Because the persistent overexpression of constitutively active C-DAAM1 was toxic to PCs, we utilized the tamoxifen-inducible FLEx CreER^{T2} system to express C-DAAM1 in PCs for short periods of time and fixed them at 12DIV. After just 6 hr of 4-OHT exposure, TdTomato-positive PCs showed little to very weak GFP signal in the dendritic shaft in both GFP and GFP-C-DAAM1 conditions (Figure 6C). However, this weak expression of GFP-C-DAAM1 was sufficient to induce a significant increase in length of dendritic protrusions (2.18 ± 0.03 μm), compared with either cultures expressing GFP for 6 hr (1.08 ± 0.02 μm) or cultures transfected with GFP-C-DAAM1, but not induced with 4-OHT (1.13 ± 0.02 μm) (Figures 6C–6E). After 12 hr of 4-OHT exposure, both GFP and GFP-C-DAAM1 could be more clearly detected in Td-Tomato-positive PCs. In contrast to GFP, GFP-C-DAAM1 showed more localization to dendritic protrusions with clear accumulation at the tips (Figures 6C and 6D). However, the dendritic protrusions by this time became very thin and dense, and many dendrites began to shrink, leaving behind blebbed membrane. Together these data show that a very small increase in the level of DAAM1 activity is sufficient to increase protrusion length, which likely better

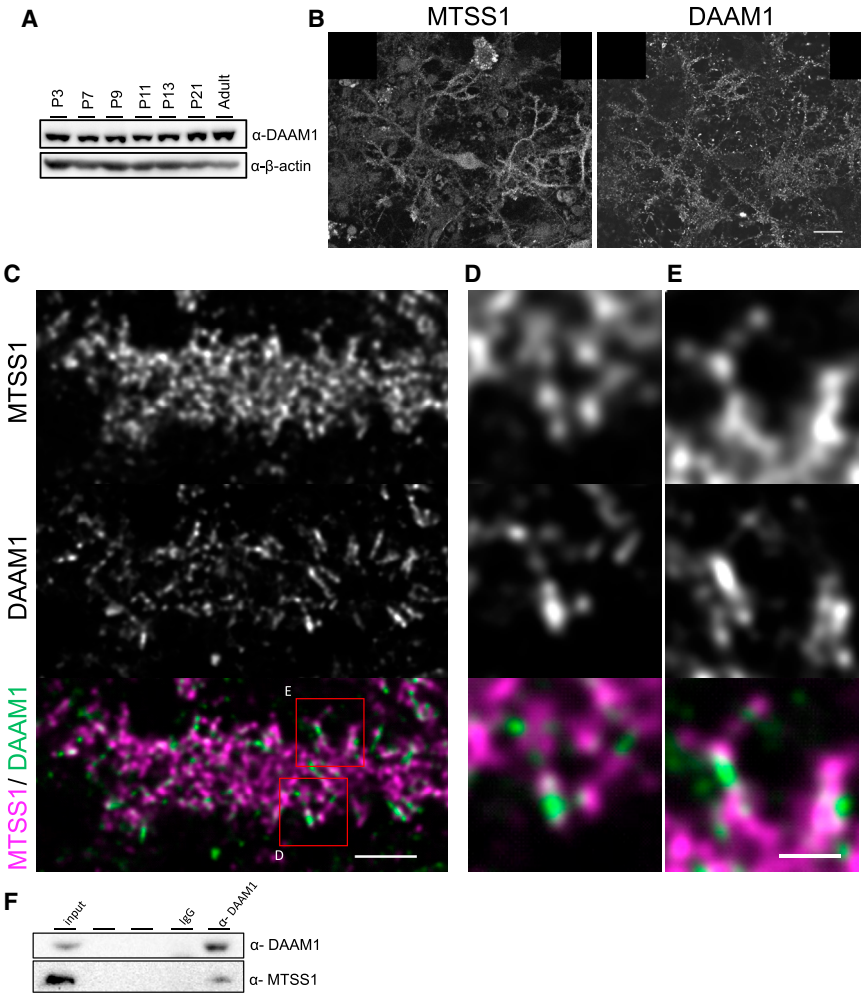

Figure 5. DAAM1 Is Localized at the Tips of Dendritic Protrusions in Developing PCs and Directly Interacts with MTSS1

(A) Western blot staining of DAAM1 from cerebellar lysates of WT mice at the indicated ages.

(B and C) Endogenous staining of MTSS1 and DAAM1 in cultured WT PCs at 12DIV at low (B) and higher (C) magnification.

(D and E) Insets shown in (C) demonstrating co-localization of MTSS1 and DAAM1 in one subset of dendritic protrusions (D) and another example (E).

(F) Immunoprecipitation from P8 cerebellar lysate with anti-DAAM1 and IgG as a negative control.

Scale bars, 20 μm (B); 3 μm (C); 1 μm (D and E). See also Figure S4.

reflects endogenous expression levels, and increasingly higher levels can lead to major disruption of cell morphology.

MTSS1 Negatively Regulates Constitutively Active DAAM1-Dependent F-Actin Elongation

To understand in better detail how MTSS1 may be negatively regulating DAAM1 activity, we used total internal reflection fluorescence (TIRF) microscopy to directly visualize DAAM1-dependent F-actin elongation, using a simplified system of DyLight488-labeled actin, profilin, and bead-immobilized C-DAAM1, with or without the presence of MTSS1 (Figures S5A–S5C). While we observed processive elongation of actin filaments from beads conjugated with GST-C-DAAM1, in the presence of purified C-MTSS1ΔWH2, the elongation speed tended to slightly decrease, and in a few filaments elongation stopped all together, resulting in a significant decrease in total elongation. We further analyzed the interplay of MTSS1 and DAAM1 in a more natural environment than cell-free assays using single-molecule speckle microscopy (SiMS) in XTC cells (Higashida et al., 2004, 2008). XTC cells form very wide, thin lamellipodia on poly-L-lysine-coated glass coverslips, allowing little obstruction from other planes of focus. Expression of very low levels of fluorophore-tagged formins allows for resolution of individual active formin dimers as speckles that show a directional movement at a constant speed, processively adding G-actin to the barbed end of an F-actin filament.

Expression of GFP-C-DAAM1 alone showed speckles with fast, directional movement (Figures 7A and 7C; Videos S4 and S5) consistent with its processive elongating activity previously reported (Jaiswal et al., 2013). In sharp contrast, coexpression of GFP-C-DAAM1 with mCherry-MTSS1 resulted in a global slowing and pausing of GFP-C-DAAM1, suggesting that the actin elongation activity of C-DAAM1 is strongly inhibited by MTSS1 (Figures 7B and 7D). Analysis of total distance traveled by each speckle during observation, which represents the length of the F-actin filament polymerized, showed that coexpression with MTSS1 reduced C-DAAM1-dependent F-actin polymerization by 48% ± 5% (Figure 7E). This inhibition of C-DAAM1-dependent F-actin elongation could similarly be achieved with C-MTSS1 (−51% ± 5%). Furthermore, coexpression of GFP-C-DAAM with C-MTSS1ΔWH2 resulted in slightly less but significant reduction in total distance traveled (−37% ± 3%).

When looking at traces of total distance traveled versus time for individual speckles, the pausing of GFP-C-DAAM1 speckles in the presence of MTSS1 and its truncates became more apparent (Figure 7F; Video S5). Therefore, we separated and quantified the speed of polymerization and state of polymerization activity. In the presence of MTSS1 and C-MTSS1, the average processive elongation speed of GFP-C-DAAM1 speckles showed strong negative correlation with mCherry-construct expression (MTSS1, $r^2 = 0.85$, $p < 0.0001$; C-MTSS1, $r^2 = 0.81$, $p < 0.0001$) (Figure 7G); however, C-MTSS1ΔWH2 did not show such correlation ($r = 0.32$, $p = 0.28$). This suggested that the slowing of elongation speed may be due to transient interference or competition of the G-actin-binding WH2 domain with C-DAAM1-dependent actin

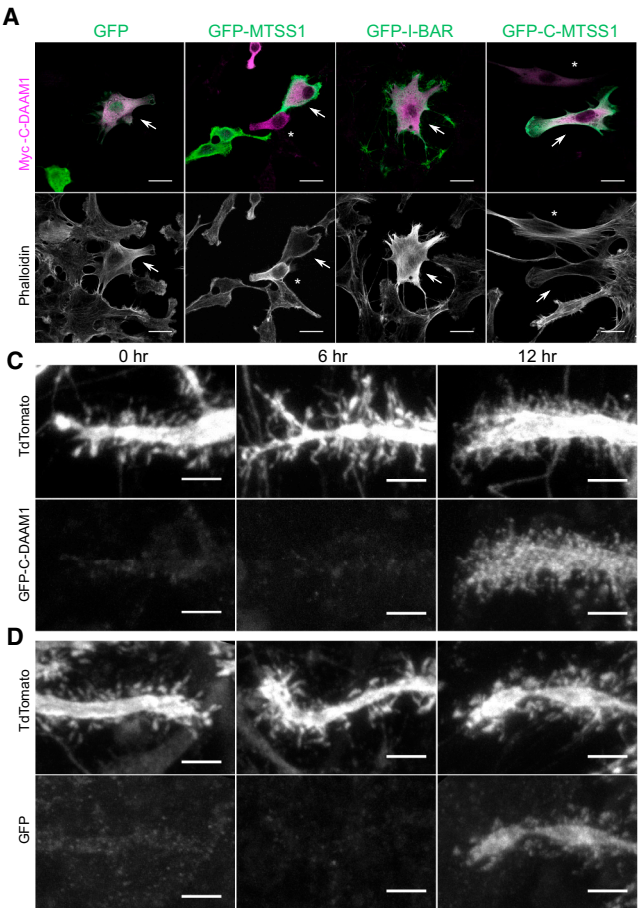

Figure 6. MTSS1 Negatively Regulates Constitutively Active DAAM1-Dependent F-Actin Elongation

(A) Representative images of NIH 3T3 cells transfected with myc-C-DAAM1 and GFP, GFP-MTSS1, GFP-I-BAR, or GFP-C-MTSS1, and stained with anti-myc, anti-GFP, and phalloidin. Arrows indicate co-transfected cells. Asterisks indicate higher relative myc-C-DAAM1-expressing cells.

(B) Quantification of phalloidin staining intensity in myc- and GFP double-positive cells described in (A) versus non-transfected cells in the same image. n = 25 for each condition.

(C and D) Representative images of dendrite segments from cultured WT PCs at 12DIV induced with 500 nM 4-OHT for the indicated times prior to fixation. PCs were transfected at 0DIV with a 1:2:3 ratio mix of CAG::TdTomato, Pcp2(L7):: CreER^{T2}, and CAG::FLEx-GFP-C-DAAM1 (C) or -GFP (D).

(E) Quantification of dendritic protrusions from PCs as described in (C) and (D).

All data show mean ± SEM. Scale bars, 20 μm (A); 3 μm (C and D). ****p < 0.0001.

elongation (Mattila et al., 2003). We further confirmed that this reduction in F-actin processive elongation was a non-specific effect of the WH2 domain by co-expressing a constitutively active mDia1 construct in the presence of an excess of MTSS1 (Figures S5D and S5E).

We next quantified the fraction of measured speckles showing pauses longer than 1 s and recovering movement on the same vector within our 20-s observation window. In control cells, an average of 9.7% ± 2.5% of GFP-C-DAAM1 speckles showed a pause of >1 s (Figure 7H). However, the proportion of GFP-C-DAAM1 speckle pausing increased and showed a significant positive correlation with MTSS1 (r^2 = 0.68, p < 0.0001) or C-MTSS1 expression level (r^2 = 0.66, p < 0.0001). This pausing behavior was independent of the WH2 domain, because coexpression with C-MTSS1ΔWH2 increased speckles showing >1-s pauses with a similar strong positive correlation (r^2 = 0.72, p < 0.0001). Furthermore, this pausing behavior was not observed when constitutively active mDia1 was cotransfected with MTSS1 (r^2 = 0.02, p = 0.52) or C-MTSS1ΔWH2 (r^2 = 0.06, p = 0.25) (Figure S5F). Thus, the above results suggest that MTSS1 negative regulation of DAAM1 does not specifically affect the incorporation speed of free G-actin into the actively elongating F-actin filament; however, MTSS1 induces pauses in actively processive DAAM1 molecules.

DISCUSSION

Here, we identified MTSS1 as an important morphological regulator of the intricate dendritic branches of cerebellar PCs. Using both cultured PCs and computer modeling characterized by contact-dependent growth inhibition, we demonstrated that simple lengthening of dendritic protrusions significantly affected final dendritic morphology. We identify MTSS1 as an endogenous formin inhibitor in vertebrate neurons that negatively regulates the dendritic protrusion-localized formin DAAM1.

Regulation of PC Morphology by MTSS1

We previously observed that dendritic filopodia act as the mediators of contact-dependent retraction of PC dendrites (Fujishima et al., 2012) and, due to their high density in developing PCs, may possibly function to extend the diameter of dendritic reach without compromising dendritic volume (Ziv and Smith, 1996). Our present observations suggest oversensitivity of the self-autonomous dendritic self-avoidance program with MTSS1 loss, and that the signaling threshold for contact-dependent retraction is not only dependent on the surface molecules expressed, but also on the physical morphology and dynamics of subcellular structures.

MTSS1 deficiency appeared not to affect differentiation of filopodia into spines, but rather caused elongation of all protrusions. This all-encompassing change in protrusion morphology is not surprising for two reasons: (1) dendritic filopodia and spines share common molecular characteristics, with dendritic filopodia containing unbundled, bidirectional F-actin filaments and actin-binding proteins similar to what are found in thin spines and the spine neck (Korobova and Svitkina, 2010); and (2)

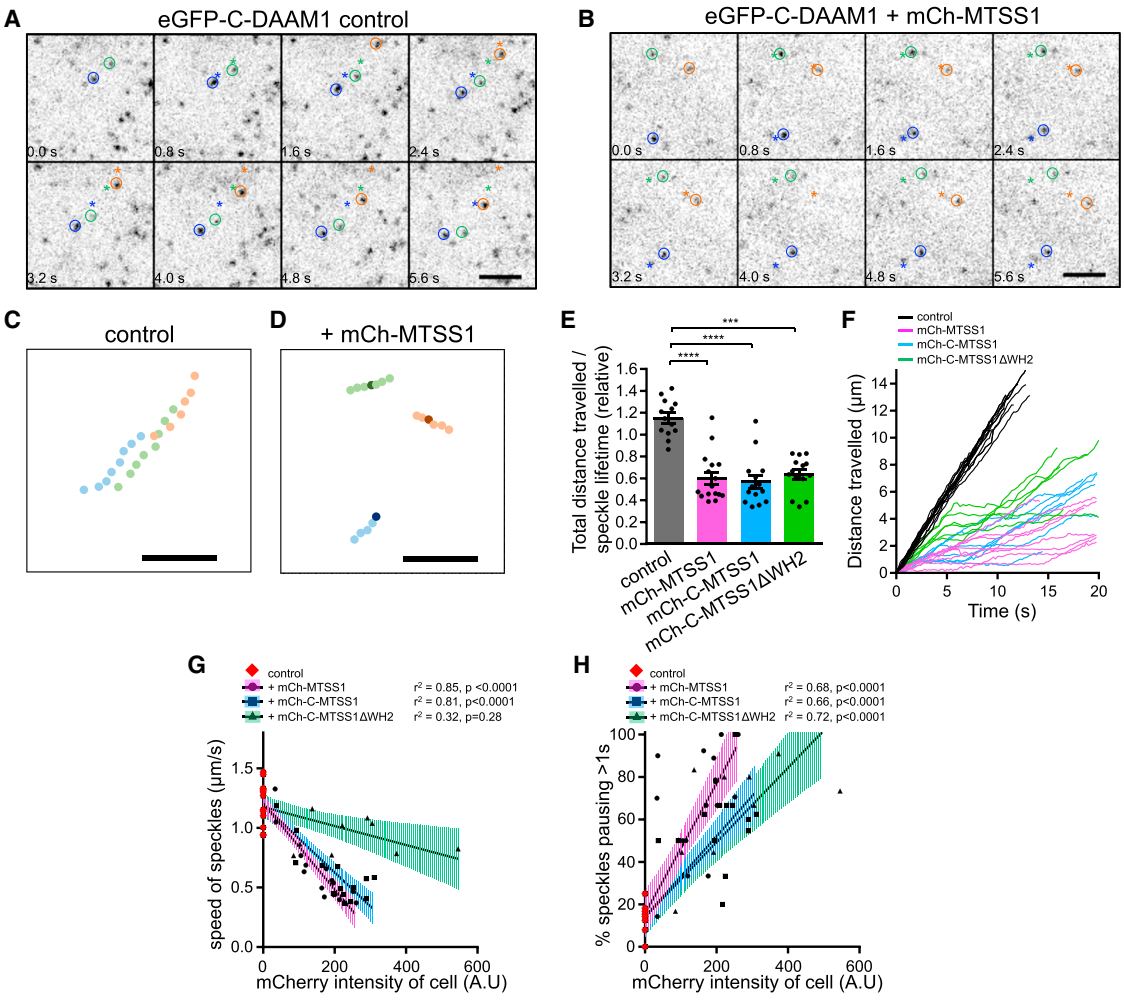

Figure 7. MTSS1 Reduces DAAM1 Actin Polymerization via Multiple Mechanisms

(A and B) SiMS imaging showing GFP signal in live XTC cells transfected with either GFP-C-DAAM1 alone (A) or with mCherry-MTSS1 (B). Asterisks indicate starting position of GFP-C-DAAM1 speckle during observation, and circles indicate the traced speckle.

(C) Speckle position per frame from images in (A).

(D) Speckle position per frame from images in (B). Darker color indicates speckle pause.

(E) The total distance traveled during observation of 10–20 GFP-C-DAAM1 speckles was averaged per cell (one data point) and normalized to the GFP-C-DAAM1 alone condition. Data show mean ± SEM.

(F) Examples of time versus distance traveled traces of individual GFP-C-DAAM1 speckles.

(G) Linear regression shows a change in GFP-C-DAAM1 speckle speed dependent on MTSS1 or C-MTSS1 expression, but not C-MTSS1ΔWH2. Speed was calculated from non-paused portions of a speckle's trace.

(H) Linear regression shows a change in proportion of measured speckles per cell showing a pause >1 s during observation dependent on expression level of all MTSS1 constructs.

Error bars indicate 95% confidence interval of linear regressions in (G) and (H). Scale bars, 5 μm. ***$p < 0.001$; ****$p < 0.0001$. See also Figure S5 and Videos S4 and S5.

dendritic protrusions lie on a reversible morphological spectrum and can show intermediate morphology between the long, thin, filopodia-like spine and the bulbous, mushroom-like spine (Nägerl et al., 2004; Schätzle et al., 2011). Thus, MTSS1 may function as one regulator of the balance of these actin-binding proteins in dendritic protrusion morphogenesis.

Dual Function of MTSS1 in Local Actin Regulation

In PCs, overexpression of MTSS1 in a WT background resulted in bulbous protrusions, which was lost by ARP2/3 inhibition, confirming that the MTSS1-ARP2/3 axis of regulation is also present in PCs. MTSS1 has been identified to indirectly upregulate the ARP2/3 pathway via two methods: (1) accumulation of the membrane phospholipid PIP_2 via its I-BAR domain, which in turn recruits ARP2/3-activating factors during initiation of dendritic protrusions (Maddugoda et al., 2011; Saarikangas et al., 2015); and (2) by interaction via its PRD with cortactin and facilitation of cortactin's upregulation of ARP2/3 activity (Lin et al., 2005).

The increase in protrusion length in MTSS1-deficient cells may be attributed to the loss of MTSS1-mediated ARP2/3 activation,

which induces compensatory formin activation and/or the loss of MTSS1-directed formin suppression. Our present results indicate a novel function of MTSS1 as a direct inhibitor of DAAM1, thus providing support for the latter scenario and suggesting MTSS1 plays a dual role as ARP2/3 activator and formin inhibitor in dendritic protrusions.

Previous studies using rat hippocampal neurons have shown MTSS1 loss resulted in a reduction of thin spine density (Saarikangas et al., 2015). The authors demonstrated that MTSS1's I-BAR domain was sufficient for abrogating this loss, leading to the conclusion that the membrane-binding function of MTSS1 is critical for filopodia initiation in hippocampal neurons. However, the authors further noted that a complete loss in protrusion initiation was not observed, possibly because of the redundant behavior of other I-BAR or F-BAR proteins. In line with this conjecture, we observed that MTSS1 loss in mouse PCs did not affect total protrusion density, nor was the I-BAR domain required for attaining proper morphology. We think this may be due to the expression of other I-BAR domain proteins such as ABBA/MTSS1L in PCs (see *in situ* hybridization data from the Allen Mouse Brain Atlas: Mtss1l - RP_050510_01_C01).

Another possibility of the morphological discrepancy may be because of our selective ablation of MTSS1 in PCs, rather than the previous global MTSS1 null animals used. Because MTSS1 is widely expressed in the CNS (Holst et al., 2008), deficiency might affect circuit formation or function, thus having a more severe effect in global knockout mice.

Taken together, we surmise that MTSS1 has dual function during dendritic protrusion formation: the first initiation step, in which the MTSS1 I-BAR domain contributes to membrane bending and ARP2/3 recruitment; and the growth step, based on a balance of DAAM1 inhibition and possibly ARP2/3 activation by the C-terminal domain.

Functional Significance of DAAM1 in Neuronal Dendritic Protrusions

We showed that acute over-activation of DAAM1 leads to transient increase in dendritic protrusion length. This is in line with previous results showing that expression of a constitutively active form of mDia2 results in an increase in filopodia length (Hotulainen et al., 2009). Experimental and computer modeling have shown that dendritic protrusion dynamics and final morphology are most dependent on the rate of actin polymerization (Marchenko et al., 2017; Miermans et al., 2017), suggesting the contribution of a concerted effort of local formin activation and release of inhibition.

We demonstrate that MTSS1 homeostatically inhibits DAAM1 actin polymerizing activity in PC dendritic protrusions. Formin activity is tightly regulated by the autoinhibitory interactions of DAD with the N-terminal diaphanous inhibitory domain (DID), which can be released by Rho family GTPases (Higashi et al., 2008), Wnt-dependent binding to Disheveled (Habas et al., 2001; Liu et al., 2008), and a yet uncharacterized conformation change of the FH2 domain to allow exposure of its actin-binding surfaces (Lu et al., 2007). We showed that MTSS1 binds to the active form of DAAM1 and inhibits actin nucleation via two mechanisms. First, overexpression of MTSS1 can non-specifically slow actin polymerization by DAAM1 and other formins via WH2-dependent competition for G-actin. This may be specifically enhanced for DAAM1 due to binding of MTSS1 and increased proximity of its WH2 domain. Second, MTSS1 can specifically induce pauses of DAAM1 during polymerization independently of the MTSS1 WH2 domain. Similar transient arrest of processive actin assembly has also been reported for Formin2 (FMN2) in the presence of its modulator Spire (Montaville et al., 2014). It has been proposed that Spire competitively binds to the barbed end of actin filaments and reversibly inhibits FMN2-induced actin nucleation. Although Spire function is complex and its molecular structure is very different from MTSS1, MTSS1 has also been shown to interact with both G-actin (Mattila et al., 2003) and F-actin (Lin et al., 2005), and may transiently interfere with other actin-binding proteins. Whether MTSS1 induces transient disassociation of the DAAM1 dimer from the F-actin, blocks G-actin addition, or prevents the sliding of the DAAM1 dimer to remain at the barbed end are just a few of the many questions that entail further study.

In conclusion, we have shown that MTSS1 modulation of opposing actin nucleation pathways is important for both macroscale and microscale morphogenesis of neuronal dendrites. Much remains to be clarified of the regulatory interplay and control of the fine actin-based temporal dynamics, which is made especially challenging because of the functional redundancy and mutual competition and/or compensation of actin binding proteins. Furthermore, observations that some formins are unable to incorporate GFP-actin in formin-assembled actin structures (Chen et al., 2012) call for careful future dissection of the function of formins in neuronal dendritic protrusions.

STAR★METHODS

Detailed methods are provided in the online version of this paper and include the following:

- KEY RESOURCES TABLE
- CONTACT FOR REAGENT AND RESOURCE SHARING
- EXPERIMENTAL MODEL AND SUBJECT DETAILS
  - Mice
  - MTSS1 cKO Mice
  - Primary Cell Culture
  - Cell Lines
- METHOD DETAILS
  - Plasmids and Construction
  - AAV Production
  - AAV Intracerebellar Injection
  - Genotyping
  - PC Electroporation
  - Pharmacological Experiments
  - Immunocytochemistry/Immunohistochemistry
  - Induced Expression of Constitutively Active C-DAAM1
  - Immunoprecipitation and Western Blot Analyses
  - Protein Purification
  - GST-Pull-down
  - Image Acquisition
  - XTC Cell Electroporation and Preparation for SIMS Imaging
  - TIRF Imaging of C-DAAM1-Dependent Elongation of F-Actin

SUPPLEMENTAL INFORMATION

Supplemental Information includes five figures and five videos and can be found with this article online at https://doi.org/10.1016/j.celrep.2018.06.013.

ACKNOWLEDGMENTS

We are grateful to Prof. Noriyuki Kioka, Dr. Yoshie Fujiwara, Dr. Sawako Yamashiro, and Naoya Hino (Kyoto University) for their expertise and recommendations on biochemical experiments; Prof. Hisanori Horiuchi (Tohoku University, Japan) and Prof. Michisuke Yuzaki (Keio University, Japan) for genetic constructs; and Junko Kurisu for her technical assistance. This work was supported by KAKENHI grants from the Japan Society for the Promotion of Science (JSPS) (16H06484 to M.K., JP16H04676 to M.M., and 16K18363 to K.F.), Japan Science and Technology Agency CREST grant JPMJCR15G5 (to N.W.), a JSPS Fellowship for Young Scientists (16J11619 to K.K.G.), and by the iCeMS Analysis Center.

AUTHOR CONTRIBUTIONS

Conceptualization, M.K. and K.K.G.; Methodology, M.K., N.W., M.M., H.M., K.F., T.U., K.S., and K.K.G.; Software, N.W. and K.F.; Validation, M.K., N.W., and K.K.G.; Formal Analysis, K.K.G., K.F., and H.M.; Investigation, K.K.G., K.F., H.M., and S.-J.L.; Resources, M.K., N.W., M.M., T.U., and K.F.; Writing, K.K.G. and M.K.

DECLARATION OF INTERESTS

The authors declare no competing interests.

Received: January 10, 2018
Revised: May 1, 2018
Accepted: June 1, 2018
Published: July 3, 2018

REFERENCES

Bompard, G., Sharp, S.J., Freiss, G., and Machesky, L.M. (2005). Involvement of Rac in actin cytoskeleton rearrangements induced by MIM-B. J. Cell Sci. *118*, 5393–5403.

Campellone, K.G., and Welch, M.D. (2010). A nucleator arms race: cellular control of actin assembly. Nat. Rev. Mol. Cell Biol. *11*, 237–251.

Chen, Q., Nag, S., and Pollard, T.D. (2012). Formins filter modified actin subunits during processive elongation. J. Struct. Biol. *177*, 32–39.

Fuerst, P.G., Bruce, F., Tian, M., Wei, W., Elstrott, J., Feller, M.B., Erskine, L., Singer, J.H., and Burgess, R.W. (2009). DSCAM and DSCAML1 function in self-avoidance in multiple cell types in the developing mouse retina. Neuron *64*, 484–497.

Fujishima, K., Horie, R., Mochizuki, A., and Kengaku, M. (2012). Principles of branch dynamics governing shape characteristics of cerebellar Purkinje cell dendrites. Development *139*, 3442–3455.

Gibson, D.A., Tymanskyj, S., Yuan, R.C., Leung, H.C., Lefebvre, J.L., Sanes, J.R., Chédotal, A., and Ma, L. (2014). Dendrite self-avoidance requires cell-autonomous slit/robo signaling in cerebellar purkinje cells. Neuron *81*, 1040–1056.

Gombos, R., Migh, E., Antal, O., Mukherjee, A., Jenny, A., and Mihály, J. (2015). The formin DAAM functions as molecular effector of the planar cell polarity pathway during axonal development in Drosophila. J. Neurosci. *35*, 10154–10167.

Habas, R., Kato, Y., and He, X. (2001). Wnt/Frizzled activation of Rho regulates vertebrate gastrulation and requires a novel Formin homology protein Daam1. Cell *107*, 843–854.

Han, C., Wang, D., Soba, P., Zhu, S., Lin, X., Jan, L.Y., and Jan, Y.-N. (2012). Integrins regulate repulsion-mediated dendritic patterning of Drosophila sensory neurons by restricting dendrites in a 2D space. Neuron *73*, 64–78.

Higashi, T., Ikeda, T., Shirakawa, R., Kondo, H., Kawato, M., Horiguchi, M., Okuda, T., Okawa, K., Fukai, S., Nureki, O., et al. (2008). Biochemical characterization of the Rho GTPase-regulated actin assembly by diaphanous-related formins, mDia1 and Daam1, in platelets. J. Biol. Chem. *283*, 8746–8755.

Higashida, C., Miyoshi, T., Fujita, A., Oceguera-Yanez, F., Monypenny, J., Andou, Y., Narumiya, S., and Watanabe, N. (2004). Actin polymerization-driven molecular movement of mDia1 in living cells. Science *303*, 2007–2010.

Higashida, C., Suetsugu, S., Tsuji, T., Monypenny, J., Narumiya, S., and Watanabe, N. (2008). G-actin regulates rapid induction of actin nucleation by mDia1 to restore cellular actin polymers. J. Cell Sci. *121*, 3403–3412.

Hoffmann, A.-K., Naj, X., and Linder, S. (2014). Daam1 is a regulator of filopodia formation and phagocytic uptake of Borrelia burgdorferi by primary human macrophages. FASEB J. *28*, 3075–3089.

Holst, M.I., Maercker, C., Pintea, B., Masseroli, M., Liebig, C., Jankowski, J., Miething, A., Martini, J., Schwaller, B., Oberdick, J., et al. (2008). Engrailed-2 regulates genes related to vesicle formation and transport in cerebellar Purkinje cells. Mol. Cell. Neurosci. *38*, 495–504.

Hotulainen, P., and Hoogenraad, C.C. (2010). Actin in dendritic spines: connecting dynamics to function. J. Cell Biol. *189*, 619–629.

Hotulainen, P., Llano, O., Smirnov, S., Tanhuanpää, K., Faix, J., Rivera, C., and Lappalainen, P. (2009). Defining mechanisms of actin polymerization and depolymerization during dendritic spine morphogenesis. J. Cell Biol. *185*, 323–339.

Jaiswal, R., Breitsprecher, D., Collins, A., Corrêa, I.R., Jr., Xu, M.-Q., and Goode, B.L. (2013). The formin Daam1 and fascin directly collaborate to promote filopodia formation. Curr. Biol. *23*, 1373–1379.

Kaneko, M., Yamaguchi, K., Eiraku, M., Sato, M., Takata, N., Kiyohara, Y., Mishina, M., Hirase, H., Hashikawa, T., and Kengaku, M. (2011). Remodeling of monoplanar Purkinje cell dendrites during cerebellar circuit formation. PLoS ONE *6*, e20108.

Kanki, H., Suzuki, H., and Itohara, S. (2006). High-efficiency CAG-FLPe deleter mice in C57BL/6J background. Exp. Anim. *55*, 137–141.

Kim, I.H., Racz, B., Wang, H., Burianek, L., Weinberg, R., Yasuda, R., Wetsel, W.C., and Soderling, S.H. (2013). Disruption of Arp2/3 results in asymmetric structural plasticity of dendritic spines and progressive synaptic and behavioral abnormalities. J. Neurosci. *33*, 6081–6092.

Kitayama, K., Abe, M., Kakizaki, T., Honma, D., Natsume, R., Fukaya, M., Watanabe, M., Miyazaki, J., Mishina, M., and Sakimura, K. (2001). Purkinje cell-specific and inducible gene recombination system generated from C57BL/6 mouse ES cells. Biochem. Biophys. Res. Commun. *281*, 1134–1140.

Korobova, F., and Svitkina, T. (2010). Molecular architecture of synaptic actin cytoskeleton in hippocampal neurons reveals a mechanism of dendritic spine morphogenesis. Mol. Biol. Cell *21*, 165–176.

Lee, K.J., Kim, H., Kim, T.S., Park, S.-H., and Rhyu, I.J. (2004). Morphological analysis of spine shapes of Purkinje cell dendrites in the rat cerebellum using high-voltage electron microscopy. Neurosci. Lett. *359*, 21–24.

Lefebvre, J.L., Kostadinov, D., Chen, W.V., Maniatis, T., and Sanes, J.R. (2012). Protocadherins mediate dendritic self-avoidance in the mammalian nervous system. Nature *488*, 517–521.

Lin, J., Liu, J., Wang, Y., Zhu, J., Zhou, K., Smith, N., and Zhan, X. (2005). Differential regulation of cortactin and N-WASP-mediated actin polymerization by missing in metastasis (MIM) protein. Oncogene *24*, 2059–2066.

Liu, W., Sato, A., Khadka, D., Bharti, R., Diaz, H., Runnels, L.W., and Habas, R. (2008). Mechanism of activation of the Formin protein Daam1. Proc. Natl. Acad. Sci. USA *105*, 210–215.

Liu, W., Komiya, Y., Mezzacappa, C., Khadka, D.K., Runnels, L., and Habas, R. (2011). MIM regulates vertebrate neural tube closure. Development *138*, 2035–2047.

Lu, J., Meng, W., Poy, F., Maiti, S., Goode, B.L., and Eck, M.J. (2007). Structure of the FH2 domain of Daam1: implications for formin regulation of actin assembly. J. Mol. Biol. *369*, 1258–1269.

Maddugoda, M.P., Stefani, C., Gonzalez-Rodriguez, D., Saarikangas, J., Torrino, S., Janel, S., Munro, P., Doye, A., Prodon, F., Aurrand-Lions, M., et al. (2011). cAMP signaling by anthrax edema toxin induces transendothelial cell tunnels, which are resealed by MIM via Arp2/3-driven actin polymerization. Cell Host Microbe *10*, 464–474.

Marchenko, O.O., Das, S., Yu, J., Novak, I.L., Rodionov, V.I., Efimova, N., Svitkina, T., Wolgemuth, C.W., and Loew, L.M. (2017). A minimal actomyosin-based model predicts the dynamics of filopodia on neuronal dendrites. Mol. Biol. Cell *28*, 1021–1033.

Mattila, P.K., Salminen, M., Yamashiro, T., and Lappalainen, P. (2003). Mouse MIM, a tissue-specific regulator of cytoskeletal dynamics, interacts with ATP-actin monomers through its C-terminal WH2 domain. J. Biol. Chem. *278*, 8452–8459.

Mattila, P.K., Pykäläinen, A., Saarikangas, J., Paavilainen, V.O., Vihinen, H., Jokitalo, E., and Lappalainen, P. (2007). Missing-in-metastasis and IRSp53 deform PI(4,5)P2-rich membranes by an inverse BAR domain-like mechanism. J. Cell Biol. *176*, 953–964.

Matusek, T., Gombos, R., Szécsényi, A., Sánchez-Soriano, N., Czibula, A., Pataki, C., Gedai, A., Prokop, A., Raskó, I., and Mihály, J. (2008). Formin proteins of the DAAM subfamily play a role during axon growth. J. Neurosci. *28*, 13310–13319.

Miermans, C.A., Kusters, R.P.T., Hoogenraad, C.C., and Storm, C. (2017). Biophysical model of the role of actin remodeling on dendritic spine morphology. PLoS ONE *12*, e0170113.

Mishina, M., and Sakimura, K. (2007). Conditional gene targeting on the pure C57BL/6 genetic background. Neurosci. Res. *58*, 105–112.

Mizuno, H., and Watanabe, N. (2014). Rotational movement of formins evaluated by using single-molecule fluorescence polarization. In Methods in Enzymology, R.D. Vale, ed. (Academic Press), pp. 73–94.

Montaville, P., Jégou, A., Pernier, J., Compper, C., Guichard, B., Mogessie, B., Schuh, M., Romet-Lemonne, G., and Carlier, M.-F. (2014). Spire and Formin 2 synergize and antagonize in regulating actin assembly in meiosis by a ping-pong mechanism. PLoS Biol. *12*, e1001795.

Nägerl, U.V., Eberhorn, N., Cambridge, S.B., and Bonhoeffer, T. (2004). Bidirectional activity-dependent morphological plasticity in hippocampal neurons. Neuron *44*, 759–767.

Nishiyama, J., Hayashi, Y., Nomura, T., Miura, E., Kakegawa, W., and Yuzaki, M. (2012). Selective and regulated gene expression in murine Purkinje cells by in utero electroporation. Eur. J. Neurosci. *36*, 2867–2876.

Parrish, J.Z., Emoto, K., Kim, M.D., and Jan, Y.N. (2007). Mechanisms that regulate establishment, maintenance, and remodeling of dendritic fields. Annu. Rev. Neurosci. *30*, 399–423.

Quinones, G.A., Jin, J., and Oro, A.E. (2010). I-BAR protein antagonism of endocytosis mediates directional sensing during guided cell migration. J. Cell Biol. *189*, 353–367.

Rotty, J.D., Wu, C., Haynes, E.M., Suarez, C., Winkelman, J.D., Johnson, H.E., Haugh, J.M., Kovar, D.R., and Bear, J.E. (2015). Profilin-1 serves as a gatekeeper for actin assembly by Arp2/3-dependent and -independent pathways. Dev. Cell *32*, 54–67.

Saarikangas, J., Kourdougli, N., Senju, Y., Chazal, G., Segerstråle, M., Minkeviciene, R., Kuurne, J., Mattila, P.K., Garrett, L., Hölter, S.M., et al. (2015). MIM-induced membrane bending promotes dendritic spine initiation. Dev. Cell *33*, 644–659.

Schätzle, P., Ster, J., Verbich, D., McKinney, R.A., Gerber, U., Sonderegger, P., and Mateos, J.M. (2011). Rapid and reversible formation of spine head filopodia in response to muscarinic receptor activation in CA1 pyramidal cells. J. Physiol. *589*, 4353–4364.

Shimada, A., Mason, C.A., and Morrison, M.E. (1998). TrkB signaling modulates spine density and morphology independent of dendrite structure in cultured neonatal Purkinje cells. J. Neurosci. *18*, 8559–8570.

Sistig, T., Lang, F., Wrobel, S., Baader, S.L., Schilling, K., and Eiberger, B. (2017). Mtss1 promotes maturation and maintenance of cerebellar neurons via splice variant-specific effects. Brain Struct. Funct. *222*, 2787–2805.

Smith, M.B., Karatekin, E., Gohlke, A., Mizuno, H., Watanabe, N., and Vavylonis, D. (2011). Interactive, computer-assisted tracking of speckle trajectories in fluorescence microscopy: application to actin polymerization and membrane fusion. Biophys. J. *101*, 1794–1804.

Smith, C.J., Watson, J.D., VanHoven, M.K., Colón-Ramos, D.A., and Miller, D.M., 3rd. (2012). Netrin (UNC-6) mediates dendritic self-avoidance. Nat. Neurosci. *15*, 731–737.

Snider, J., Pillai, A., and Stevens, C.F. (2010). A universal property of axonal and dendritic arbors. Neuron *66*, 45–56.

Spence, E.F., Kanak, D.J., Carlson, B.R., and Soderling, S.H. (2016). The Arp2/3 complex is essential for distinct stages of spine synapse maturation, including synapse unsilencing. J. Neurosci. *36*, 9696–9709.

Spudich, J.A., and Watt, S. (1971). The regulation of rabbit skeletal muscle contraction. I. Biochemical studies of the interaction of the tropomyosin-troponin complex with actin and the proteolytic fragments of myosin. J. Biol. Chem. *246*, 4866–4871.

Suarez, C., Carroll, R.T., Burke, T.A., Christensen, J.R., Bestul, A.J., Sees, J.A., James, M.L., Sirotkin, V., and Kovar, D.R. (2015). Profilin regulates F-actin network homeostasis by favoring formin over Arp2/3 complex. Dev. Cell *32*, 43–53.

Suetsugu, S., Murayama, K., Sakamoto, A., Hanawa-Suetsugu, K., Seto, A., Oikawa, T., Mishima, C., Shirouzu, M., Takenawa, T., and Yokoyama, S. (2006). The RAC binding domain/IRSp53-MIM homology domain of IRSp53 induces RAC-dependent membrane deformation. J. Biol. Chem. *281*, 35347–35358.

Sun, L.O., Jiang, Z., Rivlin-Etzion, M., Hand, R., Brady, C.M., Matsuoka, R.L., Yau, K.-W., Feller, M.B., and Kolodkin, A.L. (2013). On and off retinal circuit assembly by divergent molecular mechanisms. Science *342*, 1241974.

Takayama, C., Nakagawa, S., Watanabe, M., Mishina, M., and Inoue, Y. (1996). Developmental changes in expression and distribution of the glutamate receptor channel δ 2 subunit according to the Purkinje cell maturation. Brain Res. Dev. Brain Res. *92*, 147–155.

Takeo, Y.H., Kakegawa, W., Miura, E., and Yuzaki, M. (2015). RORα regulates multiple aspects of dendrite development in cerebellar Purkinje cells *in vivo*. J. Neurosci. *35*, 12518–12534.

Takeuchi, T., Nomura, T., Tsujita, M., Suzuki, M., Fuse, T., Mori, H., and Mishina, M. (2002). Flp recombinase transgenic mice of C57BL/6 strain for conditional gene targeting. Biochem. Biophys. Res. Commun. *293*, 953–957.

Takeuchi, T., Miyazaki, T., Watanabe, M., Mori, H., Sakimura, K., and Mishina, M. (2005). Control of synaptic connection by glutamate receptor δ2 in the adult cerebellum. J. Neurosci. *25*, 2146–2156.

Taniguchi, M., Yuasa, S., Fujisawa, H., Naruse, I., Saga, S., Mishina, M., and Yagi, T. (1997). Disruption of semaphorin III/D gene causes severe abnormality in peripheral nerve projection. Neuron *19*, 519–530.

Vig, A.T., Földi, I., Szikora, S., Migh, E., Gombos, R., Tóth, M.Á., Huber, T., Pintér, R., Talián, G.C., Mihály, J., and Bugyi, B. (2017). The activities of the C-terminal regions of the formin protein disheveled-associated activator of morphogenesis (DAAM) in actin dynamics. J. Biol. Chem. *292*, 13566–13583.

Woodings, J.A., Sharp, S.J., and Machesky, L.M. (2003). MIM-B, a putative metastasis suppressor protein, binds to actin and to protein tyrosine phosphatase delta. Biochem. J. *371*, 463–471.

Yuste, R., and Bonhoeffer, T. (2004). Genesis of dendritic spines: insights from ultrastructural and imaging studies. Nat. Rev. Neurosci. *5*, 24–34.

Ziv, N.E., and Smith, S.J. (1996). Evidence for a role of dendritic filopodia in synaptogenesis and spine formation. Neuron *17*, 91–102.

STAR★METHODS

KEY RESOURCES TABLE

REAGENT or RESOURCE	SOURCE	IDENTIFIER
Antibodies		
Rabbit polyclonal anti-MTSS1	Novus Biologicals	CAT# NBP2-24716; RRID: AB_2716709
Mouse monoclonal anti-MTSS1	Santa Cruz Biotechnology	CAT# sc-101390; RRID: AB_1126390
Chicken polyclonal anti-GFP	Thermo Fisher Scientific	CAT# A10262; RRID: AB_2534023
Mouse monoclonal anti-GFP	Santa Cruz Biotechnology	CAT# sc-9996; RRID: AB_627695
Rabbit polyclonal anti-RFP	MBL Life Science	CAT# PM005; RRID: AB_591279
Goat polyclonal anti-DAAM1	Santa Cruz Biotechnology	CAT# sc-55929; RRID: AB_2089450
Mouse monoclonal anti-DAAM1	Novus Biologicals	CAT# H00023002-M03; RRID: AB_2089446
Mouse monoclonal anti-Calbindin	Swant	CAT# 300; RRID: AB_10000347
Mouse monoclonal anti-mDia1	BD Biosciences	CAT# 610848; RRID: AB_398167
Mouse monoclonal anti-c-Myc	Enzo	CAT# BML-SA294; RRID: AB_10541551
Goat anti-GST	GE Healthcare	CAT# 27-4577-01 RRID: AB_771432
Goat anti-Chicken Alexa Fluor 488	Thermo Fisher Scientific	CAT# A-11039; RRID: AB_2534096
Goat anti-Mouse Alexa Fluor 488	Thermo Fisher Scientific	CAT# A-11029; RRID: AB_2534088
Goat anti-Mouse Alexa Fluor 568	Thermo Fisher Scientific	CAT# A-11004; RRID: AB_2534072
Donkey anti-Mouse Alexa Fluor 647	Thermo Fisher Scientific	CAT# A-31571; RRID: AB_162542
Goat anti-Rabbit Alexa Fluor 488	Thermo Fisher Scientific	CAT# A-11034; RRID: AB_2576217
Goat anti-Rabbit Alexa Fluor 568	Thermo Fisher Scientific	CAT# A-11011; RRID: AB_143157
Donkey anti-Rabbit Alexa Fluor 647	Thermo Fisher Scientific	CAT# A-31573; RRID: AB_162542
Donkey anti-Goat Alexa Fluor 568	Thermo Fisher Scientific	CAT# A-11057; RRID: AB_2536183
Donkey anti-Goat Alexa Fluor 647	Thermo Fisher Scientific	CAT# A-21447; RRID: AB_2535864
Donkey anti-mouse HRP	EMD Millipore	CAT# AP192P; RRID: AB_92658
Donkey anti-rabbit HRP	EMD Millipore	CAT# AP182P; RRID: AB_92591
Donkey anti-goat HRP	EMD Millipore	CAT# AP180P; RRID: AB_92573

(*Continued on next page*)

Continued

REAGENT or RESOURCE	SOURCE	IDENTIFIER
ChromPure Mouse IgG	Jackson ImmunoResearch Labs	CAT# 015-000-003; RRID: AB_2337188
ChromPure Goat IgG	Jackson ImmunoResearch Labs	CAT# 005-000-003; RRID: AB_2336985
Bacterial and Virus Strains		
AAV2-CAG::eGFP	Kengaku Lab	(Fujishima et al., 2012)
BL21-CodonPlus (DE3)-RIPL *E. coli*	Agilent	CAT# 230280
Chemicals, Peptides, and Recombinant Proteins		
DMEM/F12 (1:1) 1x	GIBCO	CAT# 11320-033
DMEM (1x)	GIBCO	CAT# 11965-092
Opti-MEM (1x)	GIBCO	CAT# 31985-070
HBSS (1x)	GIBCO	CAT# 14170-112
Leibovitz's L15 medium	GIBCO	CAT# 11415-064
GlutaMAX (100x)	GIBCO	CAT# 35050-061
Penicillin Streptomycin (100x)	GIBCO	CAT# 15140-122
Fetal Bovine Serum (FBS)	GIBCO	CAT# 10270-106
Progesterone	Sigma-Aldrich	CAT# P7556
Insulin	Sigma-Aldrich	CAT# I-5500
Transferrin	Sigma-Aldrich	CAT# T1283-1G
Putrescine	Sigma-Aldrich	CAT# P5780
Selenium Dioxide	Sigma-Aldrich	CAT# S9379
Bovine Serum Albumin	Sigma-Aldrich	CAT# A3156
Poly-D-lysine	Sigma-Aldrich	CAT# P6407
AraC	Sigma-Aldrich	CAT# C1768
SMI-FH2	Sigma-Aldrich	CAT# S4826
CK-666	EMD Millipore	CAT# 182515
4-OHT	Sigma-Aldrich	CAT# H7904
IPTG	Nacalai tesque	CAT# 19742-94
DAPI	Nacalai tesque	CAT# 11034-56
Alexa Fluor 647 Phalloidin	Thermo Fisher Scientific	CAT# A-22287; RRID: AB_2620155
Protease Inhibitor Cocktail (EDTA-free)	Nacalai tesque	Cat# 03969-21
DyLight 488 NHS-Ester	Thermo Fisher Scientific	CAT# 46403
0.5 μm carboxylated polystyrene microspheres	Polysciences	CAT# 09836-15
EDC (1-Ethyl-3-(3-dimethylaminopropyl)carbodiimide Hydrochloride)	Nacalai tesque	CAT# 15022-86
Thrombin	Nacalai tesque	CAT# 33842
Critical Commercial Assays		
Neuron Dissociation Kit	Wako Pure Chemical Industries	CAT# 291-78001
Lipofectamine LTX	Thermo Fisher Scientific	CAT# L3000001
AAV Helper-Free System	Agilent	CAT# 240071
AVB Sepharose High Performance	GE Healthcare	CAT# 28-4112-01
Protein A/G PLUS-Agarose	Santa Cruz Biotechnology	CAT# sc-2003
Amersham ECL prime	GE Healthcare	CAT# RPN2232
Glutathione Sepharose 4B	GE Healthcare	CAT# 17-0756-01
p- aminobenzamidine agarose	Sigma Aldrich	CAT# A7155
KOD FX polymerase	Toyobo	CAT# KFX-101
Experimental Models: Cell Lines		
RENKA ES cell line	(Mishina and Sakimura, 2007)	Masayoshi Mishina lab
HEK293T cell line	Riken BRC Cell Bank	CAT# RCB2202

(*Continued on next page*)

Continued

REAGENT or RESOURCE	SOURCE	IDENTIFIER
NIH 3T3-3-4 cell line	Riken BRC Cell Bank	CAT# RCB1862
XTC cell line	Laboratory of Naoki Watanabe	N/A
Experimental Models: Organisms/Strains		
Mice: Slc:ICR	Japan SLC	CAT# 002225
Mice: B6-Tg (CAG-FLPe)36	RIKEN	CAT# RBRC01834
Mice: C57BL/6N	CLEA Japan	CAT# C57BL/6NJcl
Mice: MTSS1$^{flox/flox}$	Laboratory of Masayoshi Mishina	This paper
Mice: GluRd2-Cre	Laboratory of Masayoshi Mishina	(Kitayama et al., 2001)
Oligonucleotides		
BAC clone carrying C57BL/6 MTSS1 CDS	BACPAC Resources Center	RP23-400B12
Genotyping primer for flox check: "s-neocassette-f " GGAATGAGATCCGCTTTCCC	Eurofins Genomics	PCReady primer
Genotyping primer for flox check: "s-neocassette-r" TCAAGCTGCAAGTGCCAGCT	Eurofins Genomics	PCReady primer
Genotyping primer for Cre check: "d2-6aS" CAGAAGCCCTGTCTTACCGATG	Eurofins Genomics	PCReady primer
Genotyping primer for Cre check: "d2 5S" GAAAGCTGCACTCAACTCTATCC	Eurofins Genomics	PCReady primer
Genotyping primer for Cre check: "Cre P2" AAATCCATCGCTCGACCAGTTTAGTTACCC	Eurofins Genomics	PCReady primer
PCR primers for MTSS1 and DAAM1. See Methods Details	Eurofins Genomics	PCReady primer
Recombinant DNA		
Plasmid: pMC1DTpA	Masayoshi Mishina lab	(Taniguchi et al., 1997)
Plasmid: pCR2.1 TOPO	Invitrogen	CAT# K4500
Plasmid: pLFNeo	Masayoshi Mishina lab	(Takeuchi et al., 2002)
Template: Mouse MTSS1 (Full-length)	Mineko Kengaku lab	This study
Template: Mouse DAAM1 (C terminus)	Mineko Kengaku lab	This study
Plasmid: pAAV-CAG-eGFP	Mineko Kengaku lab	(Fujishima et al., 2012)
Plasmid: pCMV-ΔN3-mDia1	Naoki Watanabe lab	(Higashida et al., 2004)
Plasmid: pAAV-CAG-mCherry	Mineko Kengaku lab	(Fujishima et al., 2012)
Plasmid: pCAGGS-flex	Michisuke Yuzaki lab	(Takeo et al., 2015)
Plasmid: pCL20c-L7::ER^{T2}-Cre-ER^{T2}	Michisuke Yuzaki lab	(Nishiyama et al., 2012)
Plasmid: pGEX-4T-3	GE Healthcare	CAT# 28-9545-52
Plasmid: pCMV-tag5a	Agilent	CAT# 211175
Plasmid: pAAV-CAG::TdTomato	Mineko Kengaku lab	(Fujishima et al., 2012)
Software and Algorithms		
Purkinje cell growth model	Mineko Kengaku lab	(Fujishima et al., 2012)
Fiji (ImageJ)	http://fiji.sc	RRID:SCR_002285
Imaris	http://www.bitplane.com/imaris/imaris	RRID:SCR_007370
MetaMorph Microscopy Automation and Image Analysis Software	https://www.moleculardevices.com/Products/Software/Meta-Imaging-Series/MetaMorph.html	RRID:SCR_002368
Graphpad Prism	https://www.graphpad.com/	RRID:SCR_002798
MATLAB	https://www.mathworks.com/products/matlab/	RRID:SCR_001622
Speckle Tracker J plugin	http://athena.physics.lehigh.edu/speckletrackerj	(Smith et al., 2011)
Other		
Round microscope cover glass, 12 mm No.1	Matusnami Glass IND., LTD	CAT# C012001
Square microscope cover glass, 22 × 22 mm No.1	Matusnami Glass IND., LTD	CAT# C022221

(*Continued on next page*)

Continued

REAGENT or RESOURCE	SOURCE	IDENTIFIER
SuperFrost Micro Slide Glass	Matusnami Glass IND., LTD	CAT# S2441
27-gauge needle	Terumo	CAT# NN-27195
33-gauge needle	Terumo	CAT# NN-33195
Amicon Ultra 4 Centrifugal filter Ultracel 50K	EMD Millipore	CAT# UFC805024
SpinTrap G-25	GE Healthcare	CAT# 28-9180-04
PVDF membrane, Immobilon-FL	Millipore	CAT# IPFL00005
ProLong Gold Antifade	Thermo Fisher Scientific	CAT# P36934
ChemiDoc XRS+ System	BioRad	CAT# 1708265
Nepa Electroporation Cuvettes 2mm gap	Nepagene	CAT# EC-002S
Nepa21 Electroporator	Nepagene	CAT# NEPA21
Neon® Transfection System	Invitrogen	CAT# MPK1096

CONTACT FOR REAGENT AND RESOURCE SHARING

Further information and requests for resources and reagents should be directed to and will be fulfilled by the Lead Contact, Mineko Kengaku (kengaku@icems.kyoto-u.ac.jp).

EXPERIMENTAL MODEL AND SUBJECT DETAILS

Mice

All animals were treated in accordance with the guidelines of the Animal Experiment Committee of Kyoto University. Mice were kept in a 12 hr dark/light cycle at 23 ± 3°C/50% humidity, with standard food and water provided *ad libitum*, in group housing of up to three animals per cage. MTSS1 cKO mice and their littermates were kept in standard SPF housing. Timed-pregnancy wild-type ICR mice (Japan-SLC, Cat# Slc:ICR) were obtained 1-3 days prior to giving birth and kept in a non-SPF conventional animal facility, and used in experiments requiring only mice with wild-type backgrounds (Figures 4A, 5, and 6C–6E).

MTSS1 cKO Mice

We identified a bacterial artificial chromosome (BAC) clone RP23-400B12 prepared from the C57BL/6 strain (BACPAC Resources Center, Oakland, CA) carrying the coding sequence of *Mtss1* using basic local alignment searches against the mouse genome sequence database. The targeting vector was constructed by a PCR-based method using the BAC clone DNA as a template. The 5′ homology arms were amplified by PCR with primers 5′-CGGCCGAGCTGACTACAGCTGAATGCACA-3′ and 5′-GTGATAACTTCG TATAGCATACATTATACGAAGTTATGGATCCGTTCATTATTTCAGGGTCCGTGC-3′, and 5′-ATGTATGCTATACGAAGTTATCACA GTGGTCCTTAGCTCTTCCA-3′ and 5′-GCGGCCGCTAGTTCCAGAGTCGACAAGTCACGGAGCCAGCTCTT-3′, respectively. The amplified fragments were fused by PCR and cloned into the NotI site of pMC1DTpA (Taniguchi et al., 1997) to yield pDT-5′-arm. The 3′ homology arm was amplified by PCR with primers 5′-GAGCTCGGAGTCAGATGGCCCTCGT-3′ and 5′-GCGGC CGCTCCCAGGTGCCCTAGTGAGA-3′, and cloned into the SacI-NotI sites of pCR2.1 TOPO (Invitrogen) to yield pTOPO-3′-arm. The 1.85-kb KpnI-SacI DNA fragment carrying the *loxP* sequence and *Pgk-1* promoter-driven neomycin phosphotransferase gene (*neo*) flanked by two Flp recognition target (*frt*) sites (Takeuchi et al., 2005) was cloned into the KnpI-SacI sites of pTOPO-3′-arm to yield pTOPO-LoxP-Neo-3′-arm. The SalI-NotI DNA fragment from the pTOPO-LoxP-Neo-3′-arm was cloned into the SalI-NotI sites of the pTOPO-5′-arm to yield the pMTSS1-targeting vector. The pMTSS1-targeting vector was linearized by NotI and electroporated into the embryonic stem (ES) cell line RENKA derived from the C57BL/6 strain (Mishina and Sakimura, 2007) as described previously (Takeuchi et al., 2005). G-418 (150 μg/ml)-resistant clones were picked, and recombinant clones were identified by Southern blot hybridization analysis of BamHI- or EcoRI-digested genomic DNA using PCR-amplified 534-bp fragment, PCR-amplified 599-bp fragment, and the 0.6-kb EcoRI fragment from pLFNeo (Takeuchi et al., 2002) as 5′, 3′, and neo probes, respectively. The 5′ probe and 3′ probes were amplified by PCR using 5′-ACACCAGTAGTCAGCATACTGCCT-3′ and 5′-CATGTGTACGTAAG CATTCCCAG-3′, 5′-TAATTGGCATCGGATGGTGAGG-3′ and 5′-GCCTGTCAGCACCTGAGAGC-3′ as primers, respectively. Recombinant ES cells were injected into eight-cell stage embryos of the ICR mouse line. Resulting chimera mice were mated to B6-Tg (CAG-FLPe)36 mice, a C57BL/6 strain carrying the Flp recombinase gene under control of the CAG promoter (Kanki et al., 2006), to remove the neo cassette. The resulting mice were further crossed with C57BL/6N mice to yield $MTSS1^{+/flox}$ mice. Inducible and cerebellar PC-specific MTSS1 mutant mice were obtained by crossing $MTSS1^{+/flox}$ mice with GluRδ2-$Cre^{+/Cre}$ mice carrying the Cre gene under the control of the GluRδ2 gene promoter (Kitayama et al., 2001). Littermates derived from $MTSS1^{flox/flox}$ and $MTSS1^{flox/flox-}$; GluRδ2-$Cre^{+/Cre}$ mice on the pure C57BL/6 genetic background were used for subsequent studies. Newborn homozygous floxed MTSS1 littermates were genotyped for presence or lack of GluRδ2-Cre either on the day of birth for use in primary

cultures, or at postnatal day 7 for use in immunohistochemistry experiments. No distinction between male and female pups were made for experiments.

Primary Cell Culture

For primary cerebellar dissociated cultures, cerebella from littermates of both sexes were dissected in HBSS(GIBCO), pooled together, and dissociated using the Neuron Dissociation Kit (Wako Pure Chemical Industries). Cells were resuspended in DMEM/F12 (GIBCO) supplemented by 10% FBS (GIBCO), plated on 12 mm glass coverslips (coated with 400 μg/mL poly-D-lysine (Sigma-Aldrich) overnight) at a concentration of 2 cerebella/coverslip, and incubated for 2-3 hr at 37°C/5%CO2. Following incubation, the medium was replaced by maintenance medium containing DMEM/F12 and supplemented with 0.1 mg/ml bovine serum albumin (Sigma-Aldrich), 2.1 mg/ml glucose (Sigma-Aldrich), 2x GlutaMAX (GIBCO), 8 μM progesterone (Sigma-Aldrich), 20 μg/mL insulin (Sigma-Aldrich), 200 μg/mL transferrin (Sigma-Aldrich), 100 μM putresine (Sigma-Aldrich), 30 nM selenium dioxide (Sigma-Aldrich), 5 μM Ara-C (Sigma-Aldrich), 100 units/mL penicillin (GIBCO), and 100 μg/mL streptomycin (GIBCO). Cultures were maintained at 37°C/5%CO2, with periodic replacement of a portion of the media.

Cell Lines

HEK293T cell line

HEK293T (Riken BRC Cell Bank, RCB2202) cells were maintained at 37°C/5% CO_2 and were cultured in DMEM (GIBCO) supplemented with 10% Fetal Bovine Serum (FBS), 100 units/mL penicillin, and 100 ug/mL streptomycin. Cells were passaged every 2-3 days and maintained in plastic cell culture-treated dishes.

NIH 3T3 cell line

NIH 3T3 cells were maintained at 37°C/5% CO_2 (Riken BRC Cell Bank, RCB1862) and were cultured in DMEM supplemented with 10% FBS, 100 units/mL penicillin, and 100 ug/mL streptomycin. Cells were passaged and plated at a density of $1.5x10^4$cells/cm^2 every 3 days and maintained in plastic cell culture-treated dishes. For experiments, cells were plated on glass coverslips (Matusnami Glass IND., LTD, C012001) coated with 100 ug/mL poly-D-lysine.

XTC cell line

XTC cells were maintained at 25°C and were cultured in in 70% Leibovitz's L15 medium (GIBCO) supplemented with 10% FCS (GIBCO). Cells were passaged every 2-3 days and maintained in plastic cell culture-treated dishes. For experiments, cells were plated on glass coverslips coated with 100 ug/mL poly-L-lysine, in 70% Leibovitz's L15 medium with no serum or phenol red.

METHOD DETAILS

Plasmids and Construction

The plasmids pAAV-CAG-eGFP, pAAV-CAG-mCherry, pAAV-CAG-TdTomato, and pCMV-ΔN3-mDia1 have been previously described (Fujishima et al., 2012; Higashida et al., 2004). The plasmids pCAGGS-Flex and pCL20c-L7::ERT2-Cre-ERT2 were kindly provided by Michisuke Yuzaki of Keio University, Japan. pGEX-4T-3 (GE Healthcare), pCMV-tag5a (Agilent) were purchased.

The full coding sequence of MTSS1 (Forward: ACACGGATCCATGGAGGCTGTGATCGAGAAGGAAT, Reverse: ACACGCGGCCGCCTAAGAGAAGCGCGGTGCTGAGC) and the C-DAAM1 fragment (Forward: ACACGGATCCAAGGAAGAAAT GATGCAGACCTTAA, Reverse: ACGCGGCCGCCTATTAAAAATTAAGTTTTGTGATT) were PCR amplified from P1 mouse cerebellum cDNA and cloned into the BamHI and NotI sites of pCAGGS-GFP-MCS for CAG promoter-driven N'-tagged eGFP expression constructs. Other eGFP-tagged MTSS1 truncates were PCR amplified from pCAGGS-GFP-MTSS1 and cloned into the BamHI and NotI sites of pCAGGS-GFP-MCS using the following primers: I-BAR (Forward: ACACGGATCCATGGAGGCTGTGATCGAGAAG GAAT; Reverse: ACGCGGCCGCCTAAGAACCTTTCAAGTCCAAAATC), C-MTSS1 (Forward: ACACGGATCCAAGGACTGGGCA AAGCCAGGA; Reverse: ACACGCGGCCGCCTAAGAGAAGCGCGGTGCTGAGC), C-MTSS1ΔWH2 (Forward: ACACGGATCCAAG GACTGGGCAAAGCCAGGA; Reverse: ACGCGGCCGCCTACTTCTTCAGCTTCACGCCCCTC).

For CAG promoter-driven inducible expression constructs, eGFP-C-DAAM1 was excised from pCAGGS-GFP-C-DAAM1 and cloned into the EcoRI and NotI sites of pCAGGS-Flex. To make pCAGGS-Flex-GFP, a eGFP fragment was PCR amplified (Forward: TTGACGAATTCATGGTGAGCAAGGGCGAGGAGCTG; Reverse: ATATGCGGCCGCCTACTTGTACAGCTCGTCCATGC) and cloned into the EcoRI and NotI sites of pCAGGS-flex.

For N'-tagged GST-fusion constructs, inserts were PCR amplified from pCAGGS-GFP-MTSS1 with the following primers and inserted into the BamHI and SalI sites of pGEX-4T-3. MTSS1 (Forward: ACACGGATCCATGGAGGCTGTGATCGAGAAGGAAT; Reverse: AGAGTCGACAGAGAAGCGCGGTGCTGAGCGATCGT), I-BAR(Forward: ACACGGATCCATGGAGGCTGTGATCGAGAA GGAAT; Reverse: GTGTGTCGACAGAACCTTTCAAGTCCAAAATCACC), C-MTSS1(Forward: ACACGGATCCAAGGACTGGGCA AAGCCAGGA; Reverse: AGAGTCGACAGAGAAGCGCGGTGCTGAGCGATCGT), C-MTSS1ΔWH2 (Forward: ACACGGATCCAAG GACTGGGCAAAGCCAGGA; Reverse: GTGTGTCGACTTCTCTGGGGCTCAGGTCTGCGGGG).

For CMV-promoter driven N' tagged myc-C-DAAM1, C-DAAM1 was PCR amplified from pCAGGS-GFP-C-DAAM1 with the following primers and inserted into the NotI and HinDIII sites of pCMV-tag5a. C-DAAM1 (Forward: ACATGCGGCCGCAAGGAA GAAATGATGCAGACCTT; Reverse: CATAAGCTTTTAAAAATTAAGTTTTGTGATTGGTC).

For CAG-driven N'tagged mCherry expression constructs, mCherry constructs: MTSS1 (Forward: GACGTCGACATGGAG GCTGTGATCGAGAA; Reverse: TATAAGCTTCTAAGAGAAGCGCGGTGCTGAGCGAT), C-MTSS1 (Forward: GACGTCGACAAG GACTGGGCAAAGCCAGG; Reverse: TATAAGCTTCTAAGAGAAGCGCGGTGCTGAGCGAT), C-MTSS1ΔWH2 (Forward: GACGTC GACAAGGACTGGGCAAAGCCAGG; Reverse: TATAAGCTTCTATTCTCTGGGGCTCAGGTCTGCGG).

All constructs were sequence verified.

AAV Production

HEK293T cells were transfected using calcium phosphate with the three-plasmid Agilent Helper-Free AAV system, containing a modified expression vector pAAV-CAG::eGFP (Fujishima et al., 2012), pAAV-RC, and pAAV-Helper. After two days of growth, cells were washed in an AAV-wash buffer containing 20 mM Tris HCl (pH 8.0), 250 mM NaCl, and 10 mM MgCl2, and lysed via three rounds of freeze-thaw cycles. The lysate was centrifuged and filtered through a 0.45 μm filter. Lysates were incubated with AVB Sepharose High Performance (GE Healthcare) for 15 min at RT, washed three times with AAV-wash buffer, and eluted using a buffer containing 250 mM NaCl and 10 mM MgCl2 (pH 3.0), directly into a concentrated Tris pH 8.0 for immediately neutralization. AAV particles were concentrated using an Amicon Ultra Centrifugal filter Ultracel 50K (EMD Millipore).

AAV Intracerebellar Injection

For intracerebellar injection of AAV-CAG-EGFP into WT and cKO mice, P1 or P2 pups were anesthetized by hypothermia and positioned on a homemade stereotaxic stage made for neonatal mice. After making a small incision through the occipital skin and muscle, a 27-gauge needle (Terumo) was used to create a small hole in the bone over the cerebellar vermis. A 33-gauge needle (Terumo) attached to a microsyringe containing the AAV suspension was inserted 0.5 mm through the incision in the cerebellar vermis. Over 30 s, 1-2 μL of AAV suspension was slowly injected. The wound was then sutured, and pups were revived at 37°C and returned to the litter after 2 hr.

Genotyping

Tail clippings were digested in 50 mM NaOH for 10 min at 95C. The *MTSS1*^{flox} allele (LoxP-frt check) was identified by PCR using primers 5′-GGAATGAGATCCGCTTTCCC-3′ and 5′-GTTATCTGGGTGCGCCTGTGTAC-3′ using KOD FX polymerase kit (Toyobo).

PC Electroporation

Dissociated cerebellar cells were washed three times in Optimem (GIBCO) and resuspended in a final volume of 100 μL Optimem/cuvette (Nepagene) at a concentration of 2-3 cerebella/cuvette, with 10 μg plasmid DNA. Cells were electroporated using the Nepa21 Electroporator (NepaGene) using the following settings: Poring Pulse: 150 V, 0.8 ms pulse length, 50 ms pulse interval, 2 pulses, 10% decay rate, + polarity; Transfer Pulse: 20 V, 50 ms pulse length, 50 ms pulse interval, 5 pulses, 40% decay rate, +/− polarity. After electroporation, cells were immediately washed with DMEM/F12 supplemented by 10% FBS and plated.

Pharmacological Experiments

For pharmacological experiments, SMI-FH2 (Sigma-Aldrich) was dissolved in DMSO, diluted in media, and added to cultures for 10 min at a final concentration of 10 μM SMI-FH2 and 0.01% DMSO. CK-666 (EMD Millipore) was dissolved in DMSO, diluted in media, and added to cultures for 24 hr at a final concentration of 20 μM CK-666 and 0.01% DMSO. Equivalent volumes of media and DMSO were added to control cultures.

Immunocytochemistry/Immunohistochemistry

Antibodies were diluted in PBS containing 5% skim milk (w/v) and 0.3% Triton X-100. For immunocytochemistry, cultures were fixed for 5 min at RT in freshly prepared paraformaldehyde (4%) in 10 mM MES, 138 mM KCl, 3mM MgCl2, 2 mM EGTA, and 0.32 M sucrose (pH 6.1) solution. Coverslips were then washed, and cultures were simultaneously permeabilized and blocked with 5% skim milk (w/v) in PBS and 0.3% Triton X-100 for 1 hr at RT. Cells were labeled with primary antibodies as follows: anti-calbindin (mouse, 1:1000, Swant), anti-GFP (chicken, 1:1000, Thermo Fisher Scientific), anti-MTSS1 (rabbit, 1:500, Novus Biologicals), anti-DAAM1 (goat, 1:1000, Santa Cruz), anti-RFP (rabbit, 1:1000, MBL Life Science) in 5% skim milk/PBS-Triton X-100 (0.3%) at 4°C overnight. Cells were washed extensively in PBS-Triton X-100 (0.3%) and stained with Alexa Fluor-conjugated secondary antibodies (1:10000, Molecular Probes) at RT for 1 hr. Coverslips were washed again with PBS-Triton X-100 (0.3%) and mounted on glass slides using ProLong Gold Antifade (Thermo Fisher Scientific).

For *in vivo* analysis of PC morphology and immunohistochemistry, mice were deeply anesthetized by isoflurane, and were transcardially perfused with phosphate buffer (PB) followed by 4% paraformaldehyde (PFA) in PB. Brains were removed, and postfixed overnight in 4% PFA at 4°C. Brains were then washed of PFA with three changes of 1X phosphate buffered saline (PBS), and embedded in 3% low-temperature melting agarose. Sagittal sections were made (100 mm thick) using a vibratome (DTK-3000, Dosaka EM, Kyoto, Japan). Slices were permeabilized and blocked by incubation with 5% skim milk in PBS-Triton X-100 (0.3% v/v) over night at 4°C. Primary antibody labeling was performed in blocking buffer overnight at 4°C as follows: anti-calbindin (mouse, 1:1000, Swant), anti-GFP (chicken, 1:1000, Thermo Fisher Scientific), anti-MTSS1 (rabbit, 1:500, Novus Biologicals). After thorough washing, slices were incubated with secondary antibodies for 1 h and if needed, followed by 10 ug/mL DAPI for 10 min at RT. After washing,

slices were transferred to SuperFrost Micro slides (Matsunami) and mounted with ProLong Gold Antifade Mountant (Thermo Fisher Scientific).

Induced Expression of Constitutively Active C-DAAM1

Dissociated cerebellar cells were electroporated on 0DIV with a 1:2:3 ratio mix of three plasmids, CAG::TdTomato, pCL20c-L7::ER^{T2}-Cre-ER^{T2}, and CAG::FLEx-eGFP or CAG::FLEx-eGFP-C-DAAM1, and exposed to 500 nM 4-OHT (Sigma Aldrich) either on 11DIV11 or 12DIV for variable induction times.

Immunoprecipitation and Western Blot Analyses

For western blotting and immunoprecipitation of endogenous protein, cerebella were dissected and homogenized using a Dounce homogenizer in lysis buffer (PBS plus 0.3% Triton X-100 supplemented with EDTA-free protease inhibitor cocktail (Nacalai Tesque). Lysates were incubated on ice for 30 min, cleared by centrifugation (20K x g 15 min), and either denatured for 5 min at 95°C in Laemmli buffer or used for immunoprecipitation. For immunoprecipitation, lysates were precleared for 1 hr at 4°C with Protein A/G agarose beads (Santa Cruz Biotechnologies), and then centrifuged for 500 x g for 1 min. The supernatant was incubated over night at 4°C with 5 mg of anti-DAAM1 (Novus Biologicals) or control mouse IgG antibody (Jackson ImmunoResearch Labs), followed by incubation with Protein A/G agarose beads (Santa Cruz Biotechnology) for 1 hr at 4°C. Beads were washed four times in lysis buffer and eluted in Laemmli buffer for 5 min at 95°C. Lysates and samples were separated by SDS-PAGE in 10% acrylamide gels and transferred onto PVDF membrane (Millipore). Membranes were blocked for 60 min at room temperature in PBS-Tween with 5% skimmed powdered. Membranes were incubated with primary antibodies in blocking buffer overnight at 4C at the following concentrations: anti-GFP (mouse, 1: 2000; Sant Cruz Biotechnology), anti-DAAM1 (mouse, 1:1000, Novus Biologicals), anti MTSS1 (mouse, 1:1000, Santa Cruz Biotechnology), anti-mDia1 (mouse, 1:1000, BD Biosciences). Membranes were washed and incubated for 60 min in blocking buffer containing HRP-conjugated anti- goat, rabbit or mouse secondary antibodies (1:10000; EMD Millipore). Signal was detected with ECL Prime (G.E. Healthcare) and imaged on a ChemiDoc XRS+ System (Biorad).

Protein Purification

C-DAAM1, MTSS1, and its truncates were expressed as N'tagged GST fusion proteins in BL21-CodonPlus (DE3)-RIPL-competent cells (Agilent). Cells were grown in LB medium to OD_{600} 0.6. Expression was induced by 50 μM IPTG (Nacalai tesque) for GST-MTSS1 and 250 μM IPTG for GST-C-DAAM1, GST-I-BAR, GST-C-MTSS1, and GST-C-MTSS1ΔWH2 constructs. Cells were grown at 18°C overnight for GST-MTSS1 and GST-C-DAAM1, and 37°C for 1-2 h for GST-I-BAR, GST-C-MTSS1, and GST-C-MTSS1ΔWH2 constructs. For MTSS1 and its truncates, cells were harvested and resuspended in lysis buffer (50 mM Tris HCl (pH 8.0), 150 mM NaCl, 1 mM EDTA, 10% glycerol, 1% Triton X-100, 1mM DTT, and 1 mM PMSF), with all subsequent steps performed at 4°C or on ice. Cells were lysed by sonication and centrifuged at 20k x g for 20 min. GST fusion proteins were purified by incubation with Glutathione Sepharose 4B beads (GE Healthcare) for 2 hr. The beads were then washed four times with wash buffer (50 mM Tris HCl (pH 8.0), 300 mM NaCl, 1 mM EDTA, 10% glycerol, 1% Triton X-100, 1mM DTT, and 1 mM PMSF) and eluted in glutathione buffer (50 mM Tris HCl (pH 8.0), 30 mM reduced glutathione, 150 mM NaCl). The eluted sample was concentrated using Amicon Ultra 4 Centrifugal filter Ultracel 50K (EMD Millipore) followed by buffer exchange to 50 mM Tris HCl (pH 8.0), 150 mM NaCl, 1 mM EDTA, 10% glycerol, and 1 mM PMSF using a PD-Spin Trap G-25 column (GE Healthcare). For use in total internal reflection fluorescence microscopy (TIRFM) experiments, the GST tag was cleaved from GST-C-MTSS1 ΔWH2 with thrombin (Nacalai tesque) for 1 hr at RT, and thrombin was removed by incubation with p-aminobenzamidine agarose (Sigma Aldrich). For GST-C-DAAM1, purification was performed as previously described (Vig et al., 2017), stored at 4°C, and used within two weeks.

Rabbit skeletal muscle actin was purified as previously described (Spudich and Watt, 1971), and G-actin was further purified by Superdex 200 pg HiLoad 16/60 gel filtration column (GE Healthcare). Purified G-actin was labeled with DyLight 488 NHS-Ester (Thermo Scientific) as previously described (Mizuno and Watanabe, 2014). Purification of human profilin I was previously described (Higashida et al., 2008).

GST-Pull-down

For pull-down assay, HEK293T cells were transfected with eGFP constructs using Lipofectamine LTX (Thermo Fisher). The following day, cells were washed and lysed in PBS with 0.1% Triton X-100 and EDTA-free protease inhibitor cocktail (Nacalai Tesque), passed through a 27-gauge needle 7 times, incubated on ice for 30 min, and centrifuged at 20k x g for 20 min. eGFP fluorescence per mg total protein was calculated, and lysate from untransfected cells was used to adjust for equivalent eGFP fluorescence and protein concentration between different eGFP lysates. Pull-down samples were prepared by incubating 1 mg/mL total protein concentration with equivalent eGFP fluorescence and 1 μM GST protein for 4 hr at 4°C with end-over-end rotation. Glutathione Sepharose 4B beads (GE Healthcare) were then added and further incubated for 1 hr. Samples were centrifuged at 500x g, and beads were washed four times in PBS supplemented with an additional 150 mM NaCl, 0.1% Triton X-100, and EDTA-free protease inhibitor cocktail (Nacalai Tesque). Beads were eluted in Laemmli buffer for 5 min at 95°C and separated by SDS-PAGE as described above.

Image Acquisition

For fixed samples, multi-channel fluorescent images were acquired on a Fluoview FV1000 (Olympus) laser scanning confocal microscope equipped with UPLSAPO 40x dry and 100x oil-immersion objectives (NA 0.95 and 1.40, respectively; Olympus). For *ex vivo* dendrite morphology imaging, serial confocal z stack images were acquired from midsagittal PCs in lobes IV-V with the 40x objective at a z-step of 1 μm. For *in vitro* dendrite morphology, serial confocal z stack images were acquired with the 100x objective at a z-step of 1 μm. For dendritic protrusion imaging, serial confocal z stack images were acquired at distal regions of the dendritic arbor with the 100x objective and 3x digital zoom with a voxel size of 0.04 × 0.04 × 0.39 μm.

For long-term live imaging of developing dendrites, serial confocal z stacks (4 μm stack, 5 slices x 1 μm z-step) were taken with an incubator microscope (LCV100; Olympus) equipped with a 20x objective (NA 0.7; Olympus) and CO2 supplementation. Images were taken at 3 h intervals up to 4 days.

For high-resolution live imaging of dendritic protrusions, serial confocal z stacks were taken with an incubator microscope (IX81; Olympus) equipped with a UPLSAPO 100x objective (NA 1.40, Olympus) and CO2 supplementation. Images were taken with 3x digital zoom at an interval of 15 s.

For lower-resolution multi-position live imaging of dendritic protrusions (used for the SMI-FH2 experiments), serial confocal z stacks were acquired with a spinning disk confocal microscope (CV1000; Yokogawa) using a 100x oil-immersion objective (numerical aperture 1.4; Olympus) and CO2 supplementation. Images were obtained every 30 s for 1 hr and stacked to acquire z-max projections.

For SiMS imaging, widefield images were acquired with a microscope (IX71, Olympus) equipped with 100-W mercury illumination, a PlanApo 100 × oil-immersion objective (1.40 NA; Olympus), and a cooled EMCCD camera (Evolve 512; Photometrics, Tucson, AZ). Imaging was performed at room temperature. Images were taken at 200 ms intervals for 20 s.

XTC Cell Electroporation and Preparation for SIMS Imaging

Dissociated XTC cells 1.86 × 10^5/cells were suspended in 10 μL of Buffer R of the Neon® Transfection kit (Invitrogen) with the following amounts of plasmid DNA. For the eGFP-C-DAAM1 control condition, 2.5 ng of plasmid DNA was included per 10 uL of cell suspension. For conditions co-expressing eGFP-C-DAAM1 and mCherry-MTSS1 or its mCherry-conjugated truncates, 2.5-5 ng or eGFP-C-DAAM1 and 2 μg of mCherry construct were included per 10 uL of cell suspension. Cells were electroporated using the 10 uL Neon® pipette tip using the following program: Voltage: 1005V, Width: 35 ms, Pulses: 2. For experiments, cells were trypsinization and resuspended in 70% Leibovitz's L15 medium with no serum or phenol red, and plated on glass coverslips coated with 100 μg/mL poly-L-lysine. Cells showing similar, low levels of eGFP-C-DAAM1 were selected for imaging 30 min post plating.

TIRF Imaging of C-DAAM1-Dependent Elongation of F-Actin

Two mg of 0.5 μm carboxylated microspheres (Polysciences) were functionalized with 100 μg goat anti-GST IgG (GE Healthcare) and 200 μg goat IgG (Jackson ImmunoResearch Labs) in a 3 mg/mL carbodiimide solution (Nacalai tesque) for 2 hr at RT. After quenching the reaction with glycine and extensive washing, anti-GST microspheres were incubated with purified GST-C-DAAM1 for 1 hr at 4°C. GST-C-DAAM1 beads were washed 5 times and resuspended in 50 mM KCl, 10 mM imidazole-HCl, 1 mM $MgCl_2$, 1 mM EGTA, 1 mM DTT, pH = 7.0).

DyLight 488-labeled actin was diluted with unlabeled actin to achieve 100 μL of 10% labeled actin in G-buffer (2 mM Tris-HCl, 0.2 mM $CaCl_2$, 0.2 mM ATP, and 1 mM DTT) and centrifuged at 346K x g, 4°C, for 30 min. The upper 50 μL of actin was aspirated for use in assays, within 4 hr of centrifuging.

Homemade glass flow cells were constructed as previously described (Mizuno and Watanabe, 2014), using glass coverslips that had been carbon-coated (VE-2030, Vacuum Device) and hydrophilized by "Soft" glow-discharge (PIB-10 Vacuum Device, Inc) just prior to flow cell construction. GST-C-DAAM1 beads were incubated in the flow cell for 1 min, followed by two washes of 10% BSA, incubation of 10% BSA for 5 min, and six washes of TIRF buffer (50 mM KCl, 10 mM imidazole-HCl, 1 mM $MgCl_2$, 1 mM EGTA, 50 μM CaCl2, 0.5% methylcellulose, 0.5 mM ATP, 0.5% β-mercaptoethanol, pH = 7.0).

To begin nucleation, actin-bound Ca^{2+} to Mg^{2+} exchange was performed by adding 1 mM $MgCl_2$ and 1 mM EGTA to 10% DyLight488-labeled actin in G-buffer 2 min prior to preparation and perfusion of nucleation buffer (1 μM 10% DyLight488-labeled actin, 50 mM KCl, 10 mM imidazole-HCl, 1 mM $MgCl_2$, 50 μM $CaCl_2$, 1 mM EGTA, 0.5% methylcellulose, 0.5 mM ATP, 0.5% β-mercaptoethanol, 0.1 mg glucose oxidase, 20 μg/mL catalase, 4.5 mg/mL glucose) through the flow cell. After 1 min of nucleation, four volumes of elongation buffer (0.5 μM 10% DyLight488-labeled actin, 2 μM profilin I, 50 mM KCl, 10 mM imidazole-HCl, 1 mM $MgCl_2$, 50 μM $CaCl_2$, 1 mM EGTA, 0.5% methylcellulose, 0.5 mM ATP, 0.5% β-mercaptoethanol, 0.1 mg glucose oxidase, 20 μg/mL catalase, 4.5 mg/mL glucose) with or without 5 μM C-MTSS1ΔWH2 was perfused through the flow cell. The total volume of proteins and their storing buffers were constant among samples and did not exceed 50% of the total sample buffer. All experiments were performed at 20°C.

Fluorescence images of DyLight 488-labeled actin were obtained using an IX81 microscope (Olympus) equipped with Olympus PlanApo Na 1.45100x TIRFM objective lens and BCD1 Blue DDD laser (488 nm, 20 mW, Melles Griot). Images were recorded by a CCD camera (CoolSNAP HQ, Roper Scintific) at 5 s intervals using MetaMorph software (Molecular Devices).

QUANTIFICATION AND STATISTICAL ANALYSIS

Image Analyses

For dendrite morphometry, neurons were traced in reconstructed 3-dimensional stacks using Imaris software. Sholl analysis was performed using traced dendrites with Fiji software. To illustrate the cKO phenotype, we defined a primary dendrite as any branch emerging from the soma, terminating in a bifurcation of two equivalent-thickness branches. For protrusion analysis, straight unbranching dendritic segments of 10 μm were selected at least 3 μm away from branch points and tips of dendrites. For time-lapse analysis, Z-max projections were made using Metamorph software and dendrites were reconstructed with the same methodology as the fixed samples. Protrusions were manually traced in 3-dimensional stacks using Fiji software. For fluorescent intensity analysis, the maximal intensity projected images were generated, and the mean fluorescent intensity of ROI was measured following the subtraction for off-cell background with ImageJ software (NIH).

For C-DAAM1 speckling analysis, speckles showing processive elongation movement (constant speed, same vector) were tracked using the Speckle Tracker J plugin for Fiji (Smith et al., 2011). Speckles were tracked using the "constant velocity NCC" model, and two-dimensional Gaussian fitting to identify the peak intensity of the speckle was used to improve position to subpixel accuracy. Plots of distance traveled versus time were constructed for each speckle. Due to varying lifetimes of speckles or movement of speckles out of frame, distance traveled was calculated as total distance traveled during observation divided by lifetime of speckle. Speed of speckles were calculated from the slope of the plot at regions where speckles were not obviously paused. We acknowledge that the presence of very small "non-obvious" pauses could also contribute to the reduction of speckle speed. This issue may be addressed with imaging at higher time resolution. Speckles were next classified as "paused" or "moving" at every time point. Speckles were determined to be "paused" at a time points when the total distance traveled over the preceding four frames was less than 30% of the expected distance to be traveled according to the speckle speed calculated above.

For TIRF imaging of elongating F-actin, C-DAAM1-dependent elongating F-actin were first identified by finding F-actin with one end immobilized on a bead, showing the relative dark/light regions of the F-actin being pushed away from the bead, indicating the processive incorporation of G-actin by the C-DAAM1-associated barbed end. Filaments were analyzed manually and with the KymoResliceWide plugin of Fiji.

Statistical Tests

No statistical methods were used to predetermine sample size. D'Agostino and Pearson's test was used to test for normality and to determine appropriate parametric or non-parametric tests. The unpaired two-sided Student's t test was used for isolated pairs in Figures 1C–1E, 1I, 2B–2D, 2K, 2M–2O, and S5F. Two-sided Mann-Whitney test was used for Figure 6E. Multiple paired two-sided t tests with Holm-Sidak's method was used for Figures 2G, S2A, and S2C. One-way ANOVA and Holm-Sidak's multiple comparison's test was used for Figures 6B and S3B. Kruskal-Wallis test and Dunn's multiple comparison's test was used for Figure 7E. Two-way ANOVA with Tukey's multiple comparison's test was used for Figures 3D–3F, 4B, and 4D. Linear regressions fit to Figures 7G, 7H, S5B, and S5C.

DATA AND SOFTWARE AVAILABILITY

Reconstruction of dendritic arbors by computer modeling was carried out in MATLAB software (Mathworks), as previously described (Fujishima et al., 2012) and with slight modification.

At the initial state, ten initiation sites of primary dendrites were random positioned on the surface of the cell body (a circle with a radius of 8.65 μm). At each growth step (corresponding to 3hr in experiments), every "active" dendritic terminal grew by either elongation or branching, in an alternating manner.

The elongation of dendrites was recapitulated by the addition of a dendritic unit at "active" dendritic terminals at an average rate of 0.74 times/ step. Each unit was of length L = 1.98 μm (corresponding to the average elongation speed measured by time-lapse observation of growing PC dendrites) with radius R = 2.6 (for control cells) or 3.2 (for longer dendritic protrusion cells). This dendritic unit radius reflects the radial distance from the center of the dendritic branch to the tip the filopodia, representing the radial "reach" of the dendrite. Branching of dendrites was recapitulated by the addition of two units at the growing terminal with a mean bifurcation angle of 65°, at an average rate of 0.26 times/step, which corresponds to the dichotomous branching pattern observed in growing PC dendrites.

When a growing dendritic tip collided with a neighboring branch, one of the following operations were selected and executed.

(a) Stall: Growth of the dendritic tip was terminated and became an "inactive" terminal, which would not undergo further growth or branching.
(b) Retract: The dendritic segment from the contacted tip was removed up to the nearest branch point.

Execution of either (a) or (b) was selected in a probabilistic manner, where the probability of "Stall" was determined by the quadratic $0.058T^2 - 0.0072T + 0.0054$, where T is calculation step ($1 \leq T \leq 31$). This change in the probability of Stall versus Retract corresponded to the change in retraction rate observed during PC development.